Journal of Computer-Aided Molecular Design, 10 (1996) 213–232
ESCOM

J-CAMD 340

Synthesis and conformational analysis by ^{1}H NMR and restrained molecular dynamics simulations of the cyclic decapeptide [Ser-Tyr-Ser-Met-Glu-His-Phe-Arg-Trp-Gly]

Ronald A. Buono[a], Nathalie Kucharczyk[b,*], Magrit Neuenschwander[b], Johan Kemmink[c,**], Lih-Yueh Hwang[a], Jean-Luc Fauchère[b,*] and Carol A. Venanzi[a,***]

[a]*Department of Chemical Engineering, Chemistry and Environmental Science, New Jersey Institute of Technology, 323 King Boulevard, Newark, NJ 07102, U.S.A.*
[b]*Department of Biotechnology, Swiss Federal Institute of Technology, CH-8093 Zürich, Switzerland*
[c]*Department of Biophysical Chemistry, University of Groningen, Nijenborgh 4, 9747 AG Groningen, The Netherlands*

Received 8 March 1995
Accepted 1 February 1996

Keywords: Cyclic peptides; Ester hydrolysis; Enzyme mimic; Peptide cyclization

Summary

The design of enzyme mimics with therapeutic and industrial applications has interested both experimental and computational chemists for several decades. Recent advances in the computational methodology of restrained molecular dynamics, used in conjunction with data obtained from two-dimensional ^{1}H NMR spectroscopy, make it a promising method to study peptide and protein structure and function. Several issues, however, need to be addressed in order to assess the validity of this method for its explanatory and predictive value. Among the issues addressed in this study are: the accuracy and generizability of the GROMOS peptide molecular mechanics force field; the effect of inclusion of solvent on the simulations; and the effect of different types of restraining algorithms on the computational results. The decapeptide Ser-Tyr-Ser-Met-Glu-His-Phe-Arg-Trp-Gly, which corresponds to the sequence of $ACTH_{1-10}$, has been synthesized, cyclized, and studied by two-dimensional ^{1}H NMR spectroscopy. Restrained molecular dynamics (RMD) and time-averaged restrained molecular dynamics (TARMD) simulations were carried out on four different distance-geometry starting structures in order to determine and contrast the behavior of cyclic $ACTH_{1-10}$ in vacuum and in solution. For the RMD simulations, the structures did not fit the NOE data well, even at high values of the restraining potential. The TARMD simulation method, however, was able to give structures that fit the NOE data at high values of the restraining potential. In both cases, inclusion of explicit solvent molecules in the simulation had little effect on the quality of the fit, although it was found to dampen the motion of the cyclic peptide. For both simulation techniques, the number and size of the NOE violations increased as the restraining potential approached zero. This is due, presumably, to inadequacies in the force field. Additional TARMD vacuum-phase simulations, run with a larger memory length or with a larger sampling size (16 additional distance-geometry structures), yielded no significantly different results. The computed data were then analyzed to help explain the sparse NOE data and poor chymotryptic activity of the cyclic peptide. Cyclic $ACTH_{1-10}$, which contains the functional moieties of the catalytic triad of chymotrypsin, was evaluated as a potential mimic of chymotrypsin by measurement of the rate of hydrolysis of esters of L- and D-phenylalanine. The poor rate of hydrolysis is attributed to the flexibility of the decapeptide, the motion of the side chains, which result in the absence of long-range NOEs, the small size of the macrocycle relative to that of the substrate, and the inappropriate orientation of the Gly, His, and Ser residues. The results demonstrate the utility of this method in computer-aided molecular design of cyclic peptides and suggest structural modifications for future work based on a larger and more rigid peptide framework.

*Present address: Institut de Recherches Servier, F-92150 Suresnes, France.
**Present address: European Molecular Biology Laboratory, Meyerhofstrasse 1, D-6900 Heidelberg, Germany.
***To whom correspondence should be addressed.

Introduction

In recent years there has been an enormous increase in the number of scientific studies which combine the use of NMR data with computational approaches. Torda and Van Gunsteren have reviewed the history, methodology, and utility of several molecular modeling methods which use NMR data [1] and have assessed several areas of their implementation for the promise and shortcomings of this type of methodology. Undoubtedly this approach, which allows exploration of the solution structure and function of all types of biologically active molecules, will grow in importance as advances and improvements in both the computational and experimental techniques continue.

An important class of biologically active molecules is the enzyme mimic – a relatively small, synthetic compound designed to reproduce the catalytic activity of an enzyme. To date, the design of enzyme mimics [2–27] has generally focused on the use of cyclodextrin [2–16] or macroheterocyclic [17–20] templates as the binding site, with the catalytic moieties held in place by additional molecular architecture. For serine protease mimics, only the cyclodextrin model of D'Souza et al. [14], the four-helical bundle peptide model of Hahn et al. [26] and the 29-residue cyclic peptide model of Atassi and Manshouri [28] attempt to model the complete hydrolytic reaction, although the work of Atassi and Manshouri has come under recent criticism [29–32]. Venanzi and co-workers [33–42] have used molecular mechanics and dynamics techniques to evaluate the steric and electrostatic components of molecular recognition for several of the macrocyclic serine protease mimics.

The studies described in the present paper use the cyclic decapeptide [Ser-Tyr-Ser-Met-Glu-His-Phe-Arg-Trp-Gly], i.e. ($cACTH_{1-10}$), corresponding to the first 10 residues of adrenocorticotropic hormone (ACTH). Much is known about the biological activity of ACTH [43] and of shorter linear analogs derived from the parent compound [44–50]. ^1H NMR [51] and ^{13}C NMR [52] studies have been carried out on linear analogs of ACTH. An early synthesis of $ACTH_{1-10}$ by solution methods has been described [53], while its end-to-end cyclized form has not been reported to date.

Restrained molecular dynamics (RMD) simulations [54] incorporating proton–proton distance constraints from the NMR measurements were carried out in both vacuum and solvent. The RMD technique has been used in combination with proton–proton distance constraints from two-dimensional NMR spectroscopy to determine the solution structure of peptides and proteins [55–66] as well as cyclic peptides [67–77]. In addition, the time-averaged restrained molecular dynamics (TARMD) technique of Torda et al. [78–81] was applied to $cACTH_{1-10}$ in both vacuum and solvent. This technique allows for the distance constraints to be satisfied as a time-weighted average over the trajectory and has shown to be useful when the NOE constraints result from an average of two or more conformations. In this situation, forcing the molecule to fit the NOE data with a single conformation may lead to an unphysical structure. This technique has been applied to determination of the structure of the polypeptide tendamistat [80], the protein chymotrypsin inhibitor 2 [82], and to cyclic [44,83–85] and linear [86] peptides.

The work presented here is the first step in a multiphase study of the design and synthesis of novel cyclic peptide enzyme mimics. The main focus of this first stage is the NMR and computational determination of the solution structure of the cyclic decapeptide in order to assess the utility of this methodology in computer-aided molecular design and to uncover factors which may influence the design of an optimal serine protease mimic. This work begins to investigate the use of small cyclic peptides as templates for enzyme mimic design. $cACTH_{1-10}$ was used as a starting point for what is intended to be an iterative procedure of synthesis, determination of solution structure through ^1H NMR and computer simulation, testing of enzymatic activity, and redesign of the enzyme mimic.

Materials and Methods

Chemistry

The L- and D-isomers of Boc-Phe-ONp were purchased from Sigma and checked for purity before use. The other starting materials were commercially available protected amino acids or resin-bound amino acids. The final compounds were analytically characterized at least by HPLC (single peak), amino acid analysis (AAA), except for Trp, and FAB-MS (molecular weight).

Precoated plates (Merck F254 silica gel) were used for ascending TLC in the following solvent systems (v/v): (A) $BuOH/AcOH/H_2O$ (72/7/21); (B) $CHCl_3/MeOH/H_2O/AcOH$ (85/13/1.5/0.5); (C) $CHCl_3/MeOH/H_2O/AcOH$ (70/25/4.5/0.5). Reversed-phase HPLC was performed on a Waters 625 LC system equipped with a Waters 991 photodiode array UV detector, utilizing a Deltapak C_{18} (spherical 5-mm) column (3.9 × 150 mm). Retention times, t_R, are given for isocratic or gradient elution at 1 ml/min in the

Abbreviations: AAA, amino acid analysis; Boc-L-Phe-ONp, *t*-butoxycarbonyl phenylalanyl *p*-nitophenyl ester; BOP, benzotriazol-1-yl-tris(dimethylamino)phosphonium hexafluorophosphate; But, *tert*-butyl; DCC, dicyclohexyl carbodiimide; DMF, *N,N'*-dimethylformamide; DSS, 2,2-dimethyl-2-silapentane-5-sulfonate; FAB-MS, fast atom bombardment mass spectrometry; Fmoc, (9*H*)-(fluoren-9-yl)methoxycarbonyl; HOBt, 1-hydroxybenzotriazole; HPLC, high-performance liquid chromatography; Mtr, 4-methoxy-2,3,6-trimethylbenzenesulfonyl; NMR, nuclear magnetic resonance; TFA, trifluoroacetic acid; TLC, thin-layer chromatography; Trt, triphenylmethyl.

binary solvent system (A/B) 0.1% TFA in water/0.1% TFA in acetonitrile. Preparative HPLC was routinely performed on a Waters Prep LC 3000 system equipped with a Waters 490E multiwavelength detector, on a Pre-Pak^R cartridge (47 × 300 mm) filled with a C_{18}-silica (300 Å, 15 μm) phase. Operational flow rates were 60 ml/min. For AAA, peptides were hydrolyzed in 6N HCl (0.3 ml) for 20 h at 110 °C in sealed tubes. Hydrolyzates were automatically analyzed with a Varian LC 90 Star system. The whole procedure, including liquid transfer, mixing, Fmoc derivatization, pentane extraction and separation on a Aminotag C_{18} (5-mm) column (4.6 × 150 mm) was completed within 40 min. Molecular weights of peptides were determined by FAB-MS on a Nermag R10-10C apparatus. The samples were dissolved in a glycerol/thioglycerol matrix (1:1) and ionization was effected by a beam of krypton atoms accelerated from 6 to 8 KeV. Specific optical rotations were measured (g/100 ml) on a Perkin Elmer 241 polarimeter.

Synthesis on solid phase

*c[Ser-Tyr-Ser-Met-Glu-His-Phe-Arg-Trp-Gly] (**IV**)*

The protected peptide **I** was assembled on solid phase, starting with Fmoc-Gly-sasrin-resin (2 g, 1.4 mmol, Bachem), and using a classical protocol for coupling (3 equiv of the protected amino acid, of HOBt and 3.3 equiv of DCC in 20 ml DMF and 10 ml methylene chloride), washing with DMF, isopropyl alcohol, methylene chloride (each 3× for 1 min), Fmoc removal (20% piperidine in DMF, 2× for 15 min) and washing again. Detachment of the protected peptide from the resin was achieved by treating the filtrated resin with 1% TFA in methylene chloride/anisole (19:1) for 15 min at room temperature and stopping the cleavage by addition of pyridine (1 equiv with respect to TFA). This procedure was repeated six times. The filtrates were concentrated in vacuo and the product precipitated with ether. Cleavages 3 and 4 yielded 800 mg; cleavages 2, 5 and 6 yielded 120 mg with a TLC R_f value of 0.52 (solvent system C). The solid was then stirred with 20% piperidine in DMF for 30 min at room temperature for Fmoc removal and the byproduct was extracted with pentane/ether. Overall yield of crude **II**: 620 mg (22%); TLC: R_f 0.47 (solvent system C).

For cyclization, 197 mg (0.1 mmol) of compound **II** was dissolved in 400 ml DMF and treated with 177 mg (0.4 mmol) BOP, 68 mg (0.4 mmol) HOBt and 209 μl (1.2 mmol) diisopropylethylamine. The reaction mixture was stirred for 2 h at room temperature. Evaporation of the solvent and purification of the product on Sephadex LH20 in DMF (column 2.5 × 40 cm) yielded 148 mg (75%) of **III**; TLC: R_f 0.60 (solvent system B); 0.92 (solvent system C).

For deprotection, the residue (135 mg) was suspended in 15 ml 82.5% TFA in the presence of scavengers (1 g phenol, 1 ml anisole, 500 μl ethanediol) and stirred for 4 h at 40° C. The crude product obtained after evaporation of the solvent and titration in ether (100 mg) was purified by preparative HPLC, which yielded 40 mg pure **IV** (26%); TLC R_f 0.13 (solvent system C); analytical HPLC: r_t 16 min (gradient 25 to 50% solvent system B in 50 min); $[\alpha]_D^{23} = -80.0°$ (c 1, AcOH); FAB-MS: m/e MH^+ 1281 (M = 1280); AAA: Arg 1.09 (1), Gly 1.09 (1), Glu 1.06 (1), His 1.07 (1), Met 0.97 (1), Phe 1.0 (1), Ser 1.96 (2), Tyr 0.96 (1), Trp n.d.

*Ser-Tyr-Ser-Met-Glu-His-Phe-Arg-Trp-Gly (**V**)* This compound was obtained by dissolving 100 mg of compound **II** in 15 ml 82.5% TFA in the presence of scavengers (1 g phenol, 1 ml anisole, 500 μl ethanedithiol) and stirring for 4 h at 40 °C. The crude product obtained after evaporation of the solvent and titration in ether (55 mg) was purified by preparative HPLC, which yielded 27 mg pure **V** (41%); analytical HPLC: r_t 17 min (gradient 20 to 35% solvent system B in 40 min); $[\alpha]_D^{23} = -16.1°$ (c 0.3, AcOH); FAB-MS: m/e MH^+ 1299 (M = 1298); AAA: Arg 1.08 (1), Gly 1.09 (1), Glu 1.09 (1), His 1.07 (1), Met 0.95 (1), Phe 1.0 (1), Ser 1.95 (2), Tyr 0.96 (1), Trp n.d.

Synthesis in solution

*c[Ser-Tyr-Ser-Met-Glu-His-Phe-Arg-Trp-Gly] (**IV**)*

Firstly, 145 mg (0.1 mmol) of Boc-[Glu(OBut)$_5$]ACTH$_{1-10}$ **VI** [63] was dissolved in previously cooled 90% TFA and stirred for 4.5 h at −22 °C. The solution was then poured into 150 ml diethylether (at 0 °C), after which the precipitate was filtered and washed with ether. The crude product **VII** (132 mg, 0.08 mmol), which according to TLC was only contaminated with a slight amount of the starting material, was directly dissolved in 52 ml DMF and treated with 44 mg (0.24 mmol) pentafluorophenol and 50 mg (0.24 mmol) DCC for 72 h at room temperature. Evaporation of the solvent and purification by flash chromatography on silica gel (column 3 × 40 cm) in chloroform/methanol/water/acetic acid (775:190:31:4) yielded 33 mg of ninhydrine-negative product: TLC R_f 0.13 (solvent system A, cellulose plate). The cyclic compound was then dissolved in 3 ml TFA and stirred for 20 min at room temperature. Precipitation in ether (15 ml) and filtration were then followed by treatment of the trifluoroacetate with 3 ml of 50 mM NH_4HCO_3 and by lyophilization. Yield: 29.7 mg **IV** (95%). Coelution on analytical HPLC with **IV** prepared on solid phase; $[\alpha]_D^{23} = -79.0°$ (c 1, AcOH); FAB-MS: m/e MH^+ 1299 (M = 1298); AAA: Arg 1.10 (1), Gly 1.07 (1), Glu 1.09 (1), His 1.07 (1), Met 0.95 (1), Phe 1.0 (1), Ser 1.94 (2), Tyr 0.97 (1), Trp n.d.

Analysis of hydrolysis rates

In order to analyze hydrolysis rates, 0.3 mM of the substrate Boc-L-Phe-ONp or Boc-D-Phe-ONp in 200 μl acetonitrile/ethanol/70 mM phosphate buffer (pH 7.6), volume ratio 1/12/25, was treated with decapeptide **IV** or **V** (0.2 M) and the production of *p*-nitrophenol was meas-

ured with a multiscan spectrophotometer at 405 nm as a function of time. The value in the absence of the decapeptide was obtained in the same way as with the control.

Synthesis

The key compound **IV** was obtained both by a procedure on solid phase with maximal protection of the side chains, and by a procedure in solution starting with a minimally protected known fragment of the classical synthesis of ACTH [53] in which the pentafluorophenyl ester was used for cyclization.

Compound **I** (Fig. 1) was prepared on solid phase [87] using Fmoc for N^{α}-protection and groups of the *tert*-butyl type for side-chain protection, except for the side-chains of His and Arg, for which Trt and Mtr [88] were preferred, respectively. Coupling occurred in the presence of DCC and HOBt, and N^{α}-deprotection in 20% piperidine in DMF. The side-chain-protected peptide **II** was obtained by selective cleavage (1% TFA) from the sasrin-resin especially designed for this purpose [89] and subsequent Fmoc removal. Cyclization succeeded at low concentration (0.25 mM) in DMF under activation with BOP [90] to give **III**. Final deprotection in 82% TFA in the presence of scavengers, after heating for 4 h at 40 °C in order to remove the Mtr group, afforded compound **IV**. The linear form of **IV** (compound **V**) was directly obtained from **II** under the conditions used for the removal of Mtr.

The procedure in solution (Fig. 1) started with a selective N^{α}-deprotection of the decapeptide Boc-[Glu(OBut)$_5$]-ACTH$_{1-10}$ [53] under mild acidic conditions (TFA) at low temperature (–22 °C) (splitting of Boc without loss of OBut). Cyclization was achieved via the formation of the *p*-nitrophenyl ester.

Biological testing

cACTH$_{1-10}$ was evaluated as a potential chymotrypsin mimic by measurement of the rate of hydrolysis of the substrates Boc-L-Phe-ONp and Boc-D-Phe-ONp (see above).

Spectroscopy

cACTH$_{1-10}$ was dissolved in 0.5 ml of a H_2O/D_2O mixture (90%/10%) at pH 5.0 to a final concentration of 5 mM. Proton NMR spectra were recorded on a 500 MHz spectrometer (Varian VXR500) at the University of Groningen, The Netherlands. NOESY, ROESY, and TOCSY spectra were recorded using standard pulse sequences [91–93]. The temperature was 5 °C for the buildup series and 10 °C otherwise. Mixing times varied between 50 and 450 ms for the NOESY spectra and between 50 and 300 ms for the ROESY spectra. Complete resonance assignments were obtained following Wüthrich's sequential assignment strategy [94] – no stereospecific assignments were made for methylene proton pairs. All NOEs were negative (i.e., diagonal and cross peaks in the NOESY spectra all had the same sign). No medium- or long-range NOEs could be detected. In addition, 589 'non-NOEs' were determined by the method of De Vlieg et al. [57], which converts the absence of an NOE between two protons into a minimum distance or lower bound [95] for the proton pair. A total of 39 distance restraints (39 upper and 39 lower bounds) were extracted from the assigned NOE cross peaks by carefully integrating NOE cross peaks in NOESY spectra recorded at different mixing times and extrapolating the buildup curves thus obtained to zero mixing time. These initial NOE buildup rates were calibrated using the rates obtained from tyrosine ring protons and glycine α-protons as references, assuming that the molecular motion can be described with a single correlation time, to obtain a set of distance restraints.

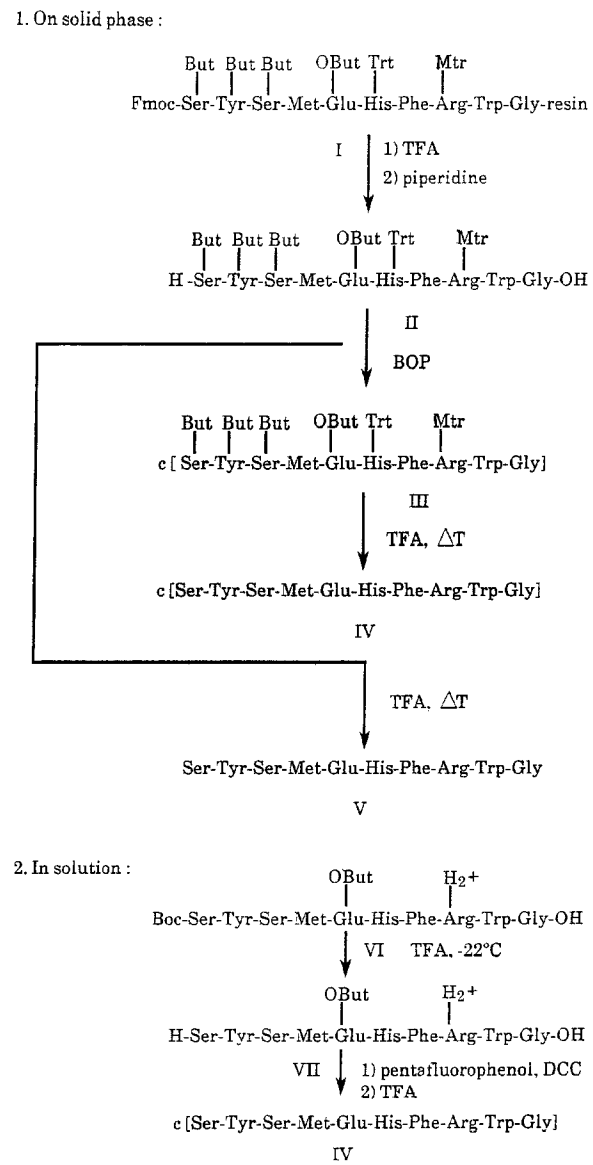

Fig. 1. Solid-phase and solution-phase synthetic scheme for compounds **I–VII**.

TABLE 1
EXCLUDED TORSION-ANGLE CONFORMATIONAL SPACE FOR THE DG1 STARTING STRUCTURE

Atom–atom[a]	Range (nm)[b]	Excluded conformational space (%)[c]
Tyr^2(H)-Ser^3(H)	0.28–0.32	84 (2)
Ser^3(H)-Met^4(H)	0.33–0.39	81 (2)
Ser^1(H)-Gly^{10}(qa2)	0.19–0.32	28 (1)
Tyr^2(H)-Ser^1(HA)	0.25–0.28	86 (1)
Tyr^2(H)-Tyr^2(HA)	0.26–0.29	64 (1)
Ser^3(H)-Tyr^2(HA)	0.20–0.23	83 (1)
Ser^3(H)-Ser^3(HA)	0.24–0.27	75 (1)
Glu^5(H)-Met^4(HA)	0.23–0.26	81 (1)
Glu^5(H)-Glu^5(HA)	0.25–0.28	69 (1)
Arg^8(H)-Phe^7(HA)	0.14–0.30	64 (1)
Arg^8(H)-Arg^8(HA)	0.26–0.29	67 (1)
Trp^9(H)-Arg^8(HA)	0.22–0.25	86 (1)
Gly^{10}(H)-Gly^{10}(qa2)	0.20–0.34	0 (1)
Tyr^2(H)-Ser^1(qb2)	0.31–0.42	62 (2)
Tyr^2(H)-Tyr^2(CG)	0.24–0.53	2 (2)
Tyr^2(H)-Tyr^2(qb2)	0.25–0.36	42 (2)
Ser^3(H)-Tyr^2(qb2)	0.28–0.39	64 (2)
Ser^3(H)-Ser^3(qb2)	0.30–0.40	14 (2)
Met^4(H)-Ser^3(qb2)	0.29–0.40	64 (2)
Met^4(H)-Met^4(qb2)	0.30–0.41	22 (2)
Met^4(H)-Met^4(qg2)	0.37–0.49	42 (3)
Glu^5(H)-Glu^5(qb2)	0.27–0.37	29 (2)
His^6(H)-Glu^5(qb2)	0.30–0.41	63 (2)
His^6(H)-Glu^5(qg2)	0.13–0.60	2 (3)
His^6(H)-His^6(qb2)	0.24–0.35	44 (2)
Phe^7(H)-Phe^7(qb2)	0.24–0.35	39 (2)
Arg^8(H)-Phe^7(qb2)	0.13–0.60	0 (2)
Arg^8(H)-Arg^8(qb2)	0.25–0.36	37 (2)
Arg^8(H)-Arg^8(qg2)	0.36–0.47	44 (3)
Trp^9(H)-Arg^8(qb2)	0.33–0.43	55 (2)
Trp^9(H)-Trp^9(qb2)	0.25–0.35	40 (2)
Tyr^2(CG)-Tyr^2(HA)	0.08–0.50	0 (1)
Tyr^2(CG)-Tyr^2(qb2)	0.12–0.53	0 (1)
Phe^7(CG)-Phe^7(qb2)	0.15–0.54	42 (1)
Phe^7(CG)-Phe^7(HA)	0.08–0.53	0 (1)
Trp^9(HE3)-Trp^9(HA)	0.29–0.32	90 (2)
Trp^9(HD1)-Trp^9(HA)	0.30–0.34	92 (2)
Trp^9(HE3)-Trp^9(qb2)	0.29–0.39	11 (1)
Trp^9(HD1)-Trp^9(qb2)	0.29–0.40	0 (1)

[a] qa2, qb2, or qg2 indicates the average position of the two protons on CA, CB, or CG, respectively.
[b] NOE constraints.
[c] Values in parentheses represent the number of nonpeptide torsional angles which determine the atom–atom distances.

Computational methods

Restrained molecular dynamics simulations and time-averaged restrained molecular dynamics simulations in vacuum and water

The 39 NOE and 589 'non-NOE' distance restraints were used as input to a modified version of the EMBED distance-geometry program [96] developed by Scheek et al. [97]. These calculations yielded a set of structures for the 92 heavy atoms of $cACTH_{1-10}$. Four of these structures which best fit the experimental data were chosen as starting structures for further study using RMD simulations. For each structure, the polar hydrogen atoms were added using the Quanta molecular modeling program [98], resulting in a total of 112 atoms per cyclic peptide. Hydrogens bonded to aliphatic carbons were treated as united atoms to decrease the number of nonbonded interactions and make the system computationally tractable. At pH 5, the pH of the NMR experiments, the aspartic acid, histidine, and arginine residues are predominantly charged. Therefore, two sets of simulations were run: a vacuum-phase calculation using the RT37C data set of amino acid structures and charges, and a solvent-phase simulation using the RT37D data set. The RT37C data set compensates for the lack of solvent screening in a vacuum-phase calculation by using neutral amino acid residues, whereas the RT37D set uses charged residues [78].

For the solvent-phase simulations, the distance-geometry structures, with added polar hydrogens, were each solvated with a water layer of 0.6 nm around all three axes. This resulted in over 700 water molecules being added to each cyclic peptide system. For both the vacuum- and solvent-phase simulations, the following procedure was used. The SHAKE algorithm [99] was applied to hold the bond lengths fixed and the force constant (k_{dc}) for the distance-constraint term in the expression for the potential energy was set at 1000 kJ/(mol nm^2) for the 39 NOEs. The four starting structures were subjected to energy minimization using the steepest descents method until the potential energy of the system changed by less than 0.001 kJ/mol. These minimized structures were then used as starting structures for the MD simulations. The initial velocities for each molecular dynamics simulation were taken from a Maxwellian distribution at 300 K. The molecule was not allowed to rotate or translate in the box. The system was weakly coupled to a thermal bath at 300 K and a pressure bath of 1 atm. The equations of motion were integrated using a time step of 2 fs by applying the algorithm of Berendsen et al. [100] with a temperature relaxation time of 0.01 ps. The value of the isothermal compressibility was taken from the work of Berendsen et al. [101]. The neighbor list of nonbonded atom pairs was updated every 10 steps. A cutoff radius of 0.6 nm was used for the list of Lennard-Jones interactions and 0.8 nm for the long-range Coulombic forces. This is similar to the methodology employed in a study of adenylate kinase, although the cutoffs are about 0.2 nm shorter [102]. A test of setting the cutoff radius at 0.8 nm for the Lennard-Jones interactions was run for the RMD vacuum simulation at 4000 kJ/(mol nm^2) (9.56 kcal/(mol Å^2)). No difference in root-mean-square (rms) deviations for the structural superpositions and torsional angle averages and variabilities (described below) was found. The RMD calculations were carried out with the 1987 version

of the GROMOS (GROningen MOlecular Simulation) package [78]. The TARMD calculations were carried out with GROMOS, supplemented with a subroutine provided by Torda. Although the united atom approach was utilized in this study, NOEs to specific protons not present in the force field were implemented with the virtual atom approach [103], which redistributes the force on the missing proton to the atoms present.

For each RMD trajectory, k_{dc} was set at 4000 kJ/(mol nm^2) for a 10-ps equilibration period and for the first 50 ps of data collection. The form of the restraining potentials used in both the RMD and TARMD simulations was half-harmonic for both lower and upper bound violations, with a flat (no force) region within the bounds. The k_{dc} value was then decreased in 10-ps intervals to 2000, 1000, 500, and 250 kJ/(mol nm^2). Data were collected for 50 ps with $k_{dc} = 0$ kJ/(mol nm^2), resulting in a total trajectory of 150 ps. For each TARMD trajectory, the memory length was set to 2.5 ps. Initially, k_{dc} was set to 4000 kJ/(mol nm^2) for a 20-ps equilibration period and for the first 80 ps of data collection. It was then decreased in 20-ps intervals to 2000, 1000, 500, and 250 kJ/(mol nm^2). Data were collected for 80 ps with $k_{dc} = 0$ kJ/(mol nm^2), resulting in a total trajectory of 260 ps. The choice of a longer trajectory for the TARMD simulations compared to the RMD simulations follows the recommendations of Torda et al. [80] and Kessler et al. [84].

Additional simulations were carried out for the TARMD vacuum simulations at $k_{dc} = 4000$ kJ/(mol nm^2) by increasing the memory length and the sampling size. To test the sensitivity of the results to the choice of memory length, 100-ps simulations (including 20 ps of equilibration) were run on each of the four distance-geometry structures with the memory length set to 5 ps. To test the sensitivity of the results to the sample size, 100-ps simulations (including 20 ps of equilibration) were run on 16 additional starting structures using a memory length of 2.5 ps. The 16 structures were obtained as follows: (i) each TARMD vacuum simulation at $k_{dc} = 4000$ kJ/(mol nm^2) and memory length 2.5 or 5 ps for each of the four distance-geometry structures (i.e. a total of eight simulations) yielded eight structures taken at 10-ps snapshot intervals; (ii) each of these eight structures was minimized to remove NOE violations; and (iii) of the eight minimized structures from each of the eight simulations, the two which exhibited the least number of NOE violations were chosen, forming a total of 16 additional starting structures.

Rms superpositioning

Rms superposition of the C^α atoms of $cACTH_{1-10}$ structures was carried out in the following manner using a program written by Scheek: (i) to see the differences between the distance-geometry starting structures (DG1, DG2, DG3, and DG4), the starting structures and the conformers obtained by minimizing them in vacuum and in solvent were superimposed on the DG1 starting structure; (ii) to see the effect of the NOE constraints on conformational variability when $k_{dc} = 4000$ or 0 kJ/(mol nm^2), conformers were selected every 5 ps during the 50- or 80-ps intervals corresponding to a particular value of k_{dc} and were superimposed on the first structure in that interval; and (iii) to determine whether the four distance-geometry structures converged to the same structure during the simulations when $k_{dc} = 4000$ or 0 kJ/(mol nm^2), conformers were selected at 10-ps intervals and were superimposed on the equilibrated DG1 structure. For steps (ii) and (iii), comparisons were made for 16 trajectories (DG1, DG2, DG3, and DG4; vacuum and solvent; and RMD and TARMD trajectories).

Substrate modeling

The Boc-Phe-ONp substrate was built using the

TABLE 2
RMS SUPERPOSITIONING RESULTS[a] FOR DISTANCE-GEOMETRY STARTING STRUCTURES[b]

DG	1	2	3	4	5	6	7	8	9	10	11	12
1	0.00	0.30	0.41	0.24	0.03	0.29	0.40	0.25	0.01	0.30	0.40	0.24
2		0.00	0.24	0.24	0.30	0.04	0.24	0.24	0.30	0.02	0.24	0.24
3			0.00	0.34	0.41	0.25	0.03	0.32	0.41	0.24	0.02	0.34
4				0.00	0.25	0.23	0.33	0.05	0.24	0.23	0.34	0.02
5					0.00	0.03	0.41	0.27	0.03	0.30	0.41	0.26
6						0.00	0.24	0.23	0.29	0.03	0.24	0.23
7							0.00	0.31	0.40	0.24	0.03	0.33
8								0.00	0.25	0.23	0.32	0.04
9									0.00	0.30	0.41	0.24
10										0.00	0.24	0.23
11											0.00	0.33
12												0.00

[a] Values are in nm.

[b] Column identifiers are: 1 = DG1; 2 = DG2; 3 = DG3; 4 = DG4; 5 = DG1 minimized in vacuum; 6 = DG2 minimized in vacuum; 7 = DG3 minimized in vacuum; 8 = DG4 minimized in vacuum; 9 = DG1 minimized in solvent; 10 = DG2 minimized in solvent; 11 = DG3 minimized in solvent; 12 = DG4 minimized in solvent.

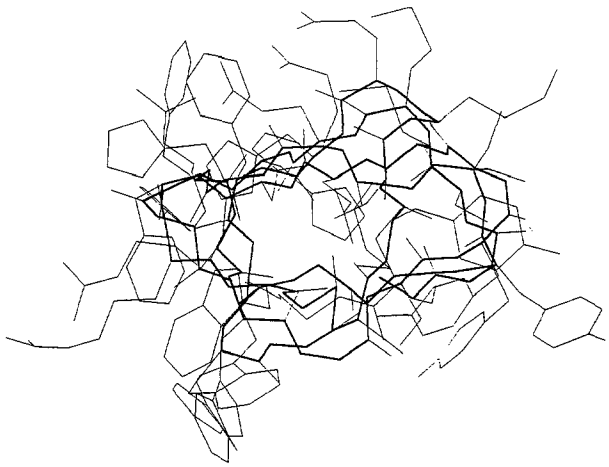

Fig. 2. Rms superposition of the DG2, DG3, and DG4 starting structures onto the DG1 starting structure. The C^{α} backbones are shown as thick lines.

CHEM-X molecular modeling program [104]. The molecule was relaxed with 20 cycles of van der Waals energy minimization and its dimensions were determined using Quanta.

Calculation of excluded torsional angle conformational space

In order to see to what extent the 39 full NOEs constrain the conformational space available to the macrocycle, a systematic check of how the proton–proton distances were affected by changes in the intervening torsional angles was manually undertaken with the Quanta modeling package. In those cases where one or two nonpeptide torsional angles determined the proton–proton distances, conformational searching was done in 30° increments, yielding a total of 12 and 144 conformations, respectively. In those cases where three nonpeptide torsional angles determined the proton–proton distances, conformational searching was done in 60° increments, yielding a total of 216 conformations. In all cases, the peptide bonds were frozen at their initial distance-geometry values. Results are expressed as the percent of the torsional angle space which has been excluded to give proton–proton distances which fall outside the range determined from the NOE data.

Results

Excluded torsional angle conformational space

Table 1 shows to what extent the NOE data excludes certain regions of static torsional angle conformational space. The DG1 starting structure is used as an example. Column one lists the proton–proton pair involved in a particular NOE and column two gives the distance range allowed for that pair. Column three gives the percent of conformational space unavailable to the torsional angles due to the restriction that they take on values which allow the proton–proton distance constraints to be satisfied. A high percentage of excluded conformational space indicates that the associated NOEs have some effect on defining the structure. The table shows that for 10 of the 39 NOEs, only 15% or less of the available torsional angle space is excluded and six have no space excluded whatsoever. This indicates that these NOEs, in particular, have little or no effect in determining the solution structure in the RMD simulations. Conversely, 9 of the 39 NOEs have at least 75% of their torsional angle space excluded and are likely to have some effect in determining the structure.

Distance-geometry structures

Table 2 gives the results of the rms superpositioning of the C^{α} atoms of the distance-geometry structures. The data in rows 1 to 4 and columns 1 to 4 give the rms deviation for the superposition of the distance-geometry starting structures on each other. The magnitudes of these numbers indicate that all four starting structures are different. For example, reading across the first row shows that DG2 compared to DG1 has an rms deviation of 0.30

TABLE 3
NOE VIOLATIONS[a] FOR DISTANCE-GEOMETRY STARTING STRUCTURES

NOE	Structure			
	DG1	DG2	DG3	DG4
Tyr^{2}(H)-Ser^{3}(H)	0.041	0.020	0.006–	0.052
Ser^{3}(H)-Met^{4}(H)		0.027–		0.008–
Tyr^{2}(H)-Ser^{1}(HA)		0.007–	0.012–	
Tyr^{2}(H)-Tyr^{2}(HA)			0.040–	0.033–
Ser^{3}(H)-Tyr^{2}(HA)		0.021	0.049	
Ser^{3}(H)-Ser^{3}(HA)	0.015–	0.011		0.012
Glu^{5}(H)-Met^{4}(HA)		0.002–		
Glu^{5}(H)-Glu^{5}(HA)	0.009–	0.004–	0.012–	0.015–
Arg^{8}(H)-Arg^{8}(HA)			0.001–	0.011–
Trp^{9}(H)-Arg^{8}(HA)	0.001–	0.010–	0.010–	0.003–
Tyr^{2}(H)-Tyr^{2}(qb2)				0.018
Ser^{3}(H)-Tyr^{2}(qb2)	0.010	0.031	0.022	
Met^{4}(H)-Ser^{3}(qb2)	0.013	0.028–	0.034–	0.004–
Met^{4}(H)-Met^{4}(qb2)				0.019–
Met^{4}(H)-Met^{4}(qg2)		0.021–	0.032–	0.005–
Glu^{5}(H)-Glu^{5}(qb2)	0.003		0.005–	
His^{6}H(H)-Glu^{5}(qb2)			0.011–	0.020–
His^{6}(H)-His^{6}(qb2)				0.016
Arg^{8}(H)-Arg^{8}(qb2)	0.002–	0.003–		
Trp^{9}(H)-Trp^{9}(qb2)	0.001			
Trp^{9}(HE3)-Trp^{9}(HA)	0.021	0.019	0.003	0.020
Total number of violations	10	13	13	14
Number of upper bound violations	6	5	3	5

[a] Violations in nm; lower bound violations are indicated with a '–' after the number; qb2 or qg2 indicates the average position of the two protons on CB or CG, respectively.

TABLE 4
SUMMARY OF NOE VIOLATIONS[a] FOR 16 ADDITIONAL DISTANCE-GEOMETRY STARTING STRUCTURES

Structure[b]	NOE violation (nm)
DG1a	15/8
DG1b	10/8
DG1c	12/5
DG1d	13/9
DG2a	12/5
DG2b	15/10
DG2c	13/7
DG2d	13/8
DG3a	10/6
DG3b	13/9
DG3c	11/7
DG3d	11/8
DG4a	15/9
DG4b	12/7
DG4c	13/8
DG4d	12/7

[a] Data expressed as the total number of violations/number of upper bound violations.

[b] As described in the text, DGs a and b are the two lowest energy-mininized structures of the eight snapshots from the simulation of DG using a 2.5-ps memory length; DGs c and d are the two lowest energy-minimized structures of the eight snapshots from the simulation of DG using a 5-ps memory length.

nm, whereas the rmsd of DG3 compared to DG1 is 0.41 nm. The difference between the structures can be seen more clearly in Fig. 2, which displays the result of the rms superposition of the DG2, DG3, and DG4 starting structures onto DG1. Rows 1 to 4 and columns 5 to 8 of Table 2 compare the structures minimized in vacuum to the distance-geometry starting structures. The results show that the structures differ little from the starting structures after minimization. For example, DG2 minimized in vacuum has an rms deviation of 0.04 nm when superimposed on the DG2 starting structure. Rows 1 to 4 and columns 9 to 12 give the rms deviation for the distance-geometry structures minimized in solvent compared to the distance-geometry starting structures. The results here also show that each distance-geometry starting structure changes little upon minimization in solvent.

Table 3 gives the magnitudes of the NOE violations of the 39 upper and 39 lower bound distance restraints for the four distance-geometry starting structures. The table shows that the structures exhibit between 10 and 14 violations with half or fewer being violations of upper bound distance constraints. The magnitudes of the NOE violations for all four structures are small (much less than 0.1 nm). Therefore, the starting structures for the simulations can be considered to satisfy the distance constraints. Table 4 summarizes the NOE violations for the 16 additional starting structures. Comparison of Tables 3 and 4 shows that the total numbers of violations are similar, but the 16 additional starting structures exhibit slightly more upper bound violations.

NOE violations

Table 5 compares the types of NOE violations of the four distance-geometry starting structures to those exhibited during the 16 trajectories. The table shows that most of the NOE violations seen during a trajectory are of the same type as exhibited by the distance-geometry starting structures, i.e. types Tyr^2(H)-Ser^3(H) to Trp^9-(HE3)-Trp^9(HA). In fact, several of the distance-geometry starting structure NOE violations appear in each of the 16 trajectories: Tyr^2(H)-Ser^3(H); Ser^3(H)-Met^4(H); Tyr^2-(H)-Ser^1(HA); Ser^3(H)-Ser^3(HA); and Trp^9(HE3)-Trp^9-(HA). It is interesting to note that, for the DG1 starting structure (Table 1), all of these were found to have most of their torsional angle space excluded.

Even though the trajectory and the starting structure for that trajectory have many common violations, the trajectory always exhibits more different types of violations than the starting structure. For example, the DG1 starting structure gives a violation for the Tyr^2(H)-Ser^3(H) distance which is maintained in each of the four simulations: vacuum RMD, solvent RMD, vacuum TARMD, and solvent TARMD. However, each of those four trajectories also gives a violation for the Ser^3(H)-Met^4(H) and Tyr^2(H)-Ser^1(HA) distances. This type of behavior is also seen at the bottom of Table 5, where eight new types of violations are listed which appear during the trajectory that are not found in any of the four starting structures. One of these, Trp^9(HD1)-Trp^9(HA), shows up in every one of the trajectories and, for the DG1 starting structure (Table 1), has 92% of its torsional angle space excluded. Conversely, there is no type of NOE violation exhibited by the distance-geometry structures which is also not exhibited by at least one of the trajectories. This is not surprising, since the DG structures were constructed without regard to internal energy and correspond to structures around 0 K, while the molecular dynamics simulations correspond to an effective temperature around 300 K. Introduction of thermal energy would be expected to increase restraint violations. For example, the Trp^9(H)-Trp^9(HB) distance is a violation in the DG1 starting structure. Although it is not a violation in the DG1 vacuum RMD, solvent RMD, and solvent TARMD trajectories, it does appear in the vacuum TARMD trajectory. In general, Table 5 shows that the simulations have explored regions of the conformational space around the distance-geometry starting structures.

Trajectories

Tables 6–9 report the total number of lower and upper bound violations and the individual NOE violations of at least 0.060 nm for the RMD vacuum, RMD solvent, TARMD vacuum, and TARMD solvent simulations, respectively. Tables 6 and 7 report proton–proton distances from the RMD simulations which were calculated based on average distances of 50-fs snapshots over the

corresponding time interval. Thus, there are 1000 data points which comprise the average values in the RMD results for the 10–60 and 100–150 ps intervals. Tables 8 and 9 report proton–proton distances of the TARMD simulations which were calculated based on the r^{-3}-weighted averages of 50-ps snapshots. There are, therefore, 1600 data points which comprise the averages in the TARMD results for the 20–100 and 180–260 ps intervals. The arbitrary value of 0.060 nm was chosen as a cutoff criterion for reporting the individual NOE violations in the tables.

The tables show that most of the NOE violations are violations of the upper bound. Relatively small NOE violations, on the order of hundredths of a nanometer, indicate that the structure satisfies the distance restraints. By contrast, violations on the order of a tenth of a nanometer which persist, or appear if k_{dc} goes to zero, indicate that the structure was simply held in place initially by the restraining potential when $k_{dc} = 4000$ kJ/mol nm^2. The change in the magnitude of the NOE violations if the restraining potential goes to zero is, therefore, one test of whether the force field is sufficiently accurate to allow the structure to satisfy the distance constraints without the imposition of a restraining potential. For the discussion below, if a trajectory shows no NOE violations greater than or equal to 0.060 nm for a particular value of k_{dc}, it is said to satisfy the distance constraints for that k_{dc}.

For the RMD vacuum simulations (Table 6), none of the trajectories satisfies the distance constraints at large values of k_{dc}. Only the DG1 trajectory comes close to satisfying the distance constraints as the restraining potential is removed. The DG2, DG3, and DG4 trajectories

TABLE 5
TYPES OF NOE VIOLATIONS IN STARTING STRUCTURES VERSUS TRAJECTORIES

NOE[a]	RMD trajectory								TARMD trajectory							
	Vacuum				Solvent				Solvent				Vacuum			
	1[b]	2	3	4	1	2	3	4	1	2	3	4	1	2	3	4
Tyr^2(H)-3 Ser(H)	C	C	C	C	C	C	C	C	C	C	C	C	C	C	C	C
Ser^3(H)-Met^4(H)	T	C	T	C	T	C	T	C	T	C	T	C	T	C	T	C
Tyr^2(H)-Ser^1(HA)	T	C	C	T	T	C	C	T	T	C	C	T	T	C	C	T
Tyr^2(H)-Tyr^2(HA)	–	–	C	+	–	T	C	C	–	T	+	C	–	–	+	C
Ser^3(H)-Tyr^2(HA)	T	C	C	T	T	C	C	–	T	+	+	–	T	C	C	T
Ser^3(H)-Ser^3(HA)	C	C	T	C	C	C	T	C	C	C	T	C	C	C	T	C
Glu^5(H)-Met^4(HA)	T	C	T	T	T	C	T	–	T	C	T	T	T	C	T	T
Glu^5(H)-Glu^5(HA)	C	+	C	+	C	+	C	C	C	+	C	C	C	C	C	C
Arg^8(H)-Arg^8(HA)	–	T	+	C	–	–	+	+	T	–	C	C	T	T	C	+
Trp^9(H)-Arg^8(HA)	C	C	+	C	C	C	C	C	C	C	C	C	C	C	C	C
Tyr^2(H)-Tyr^2(qb2)	–	–	–	C	–	–	T	C	–	–	–	+	–	–	T	+
Ser^3(H)-Tyr^2(qb2)	C	C	C	T	C	C	C	–	C	C	C	T	C	C	C	T
Met^4(H)-Ser^3(qb2)	C	+	C	+	C	+	+	+	C	C	C	+	+	+	C	C
Met^4(H)-Met^4(qb2)	T	T	T	C	–	T	T	C	T	–	T	C	T	T	–	C
Met^4(H)-Met^4(qg2)	T	C	C	C	T	+	C	C	–	C	C	C	T	C	C	C
Glu^5(H)-Glu^5(qb2)	C	T	+	–	C	T	+	–	+	T	C	–	+	T	C	–
His^6(H)-Glu^5(qb2)	T	T	C	+	–	T	C	C	–	T	+	C	–	T	C	C
His^6(H)-His^6(qb2)	T	–	–	C	T	–	–	+	T	–	T	+	–	–	–	C
Arg^8(H)-Arg^8(qb2)	C	+	–	–	C	+	–	–	C	C	–	–	C	+	–	–
Trp^9(H)-Trp^9(qb2)	+	T	–	–	+	T	–	–	+	–	–	T	C	–	–	–
Trp^9(HE3)-Trp^9(HA)	C	C	C	C	C	C	C	C	C	C	C	C	C	+	C	C
New NOE violations during trajectories																
Arg^8(H)-7 Phe(HA)	–	–	T	T	–	–	T	T	–	–	–	T	T	T	–	T
Tyr^2(H)-Ser^1(qb2)	–	–	T	–	–	T	–	–	–	–	T	-	–	–	T	–
Ser^3(H)-Ser^3(qb2)	–	–	T	–	T	T	–	T	T	T	–	T	T	–	–	T
Phe^7(H)-Phe^7(qb2)	T	–	–	T	T	–	–	–	–	–	–	T	–	T	–	–
Arg^8(H)-Arg^8(qg2)	T	T	T	T	T	T	–	T	–	T	T	T	–	T	T	–
Trp^9(H)-Arg^8(qb2)	–	T	–	–	–	T	–	–	T	T	–	T	T	T	T	–
Trp^9(HE3)-Trp^9(qb2)	–	–	–	–	T	–	T	–	–	–	T	–	–	–	–	–
Trp^9(HD1)-Trp^9(HA)	T	T	T	T	T	T	T	T	T	T	T	T	T	T	T	T

Symbols: –=no violation appeared in either the starting structure or the trajectory; +=violation(s) appeared only in the starting structure; T=one or more violations appeared for at least one value of k_{dc} only in the trajectory; C=one or more violations appeared for at least one value of k_{dc} in both the starting structure and the trajectory.

[a] qb2 or qg2 indicates the average position of the two protons on CB or CG, respectively.

[b] 1, 2, 3 and 4 indicate structures DG1, DG2, DG3 and DG4, respectively.

TABLE 6
NOE VIOLATIONS IN RMD VACUUM SIMULATIONS

Structure/NOE[a]	k_{dc} (kJ/(mol nm^2))					
	4000 (10–60)[b]	2000 (60–70)	1000 (70–80)	500 (80–90)	250 (90–100)	0 (100–150)
DG1						
Glu^5(H)-Met^4(HA)	0.075	0.078	0.078	0.083	0.080	–
Met^4(H)-Met^4(qg2)	0.072–	0.073–	0.080–	0.081–	0.064–	–
Trp^9(HE3)-Trp^9(HA)	0.136	0.139	0.147	0.141	0.137	0.060
Total violations[c]	9/8	9/8	10/8	10/9	9/8	9/5
DG2[b]						
Tyr^2(H)-Ser^3(H)	–	0.063	0.062	–	–	–
Trp^9(H)-Arg^8(HA)	0.063	0.098	0.098	0.085	0.087	0.099
Met^4(H)-Met^4(qg2)	–	–	–	–	0.085–	0.088–
Trp^9(H)-Arg^8(qb2)	–	–	–	–	0.062–	–
Trp^9(HE3)-Trp^9(HA)	0.066	–	0.144	0.077	0.093	0.070
Total violations	7/6	6/6	5/7	5/7	4/6	3/8
DG3[b]						
Tyr^2(H)-Ser^3(H)	–	0.110	0.109	0.110	0.105	0.110
Glu^5(H)-Met^4(HA)	–	–	0.067	0.075	–	–
Met^4(H)-Met^4(qg2)	–	–	0.086–	0.082–	–	–
His^{6}H(H)-Glu^5(qb2)	–	–	–	0.081–	–	–
Trp^9(HE3)-Trp^9(HA)	0.152	0.102	–	–	–	0.102
Trp^9(HD1)-Trp^9(HA)	–	–	–	0.061	–	–
Total violations	7/8	9/6	7/7	6/6	9/6	9/6
DG4[b]						
Tyr^2(H)-Ser^3(H)	0.095	0.072	0.067	0.085	0.082	0.071
Tyr^2(H)-Ser^1(HA)	0.073	0.068	0.067	0.067	0.068	0.064
Met^4(H)-Met^4(qg2)	–	–	0.065–	–	–	–
Trp^9(HE3)-Trp^9(HA)	0.077	–	0.079	0.083	0.082	0.121
Trp^9(HD1)-Trp^9(HA)	0.096	0.068	0.106	0.104	0.101	0.077
Total violations	4/6	6/5	7/5	6/6	7/7	7/6

Distances in nm; lower bound violations are indicated by a '–' following the number, numbers without this indication are upper bound violations.
[a] qb2 or qg2 indicates the average position of the two protons on CB or CG, respectively.
[b] Time interval (ps).
[c] Number of upper bound violations/number of lower bound violations.

show one or two violations on the order of 0.1 nm at k_{dc} = 0 kJ/(mol nm^2). Some NOE violations are common to the four trajectories. All have structures with NOE violations of 0.060 nm or larger for the Trp^9(HE3)-Trp^9(HA) distance at k_{dc} = 0 and 4000 kJ/(mol nm^2). The DG3 and DG4 trajectories also have NOE violations of 0.060 nm or larger for the Tyr^2(H)-Ser^3(H) distance at k_{dc} = 0 kJ/(mol nm^2).

For the solvent RMD simulations (Table 7), as for the vacuum RMD simulations, none of the four trajectories satisfies the distance constraints at k_{dc} = 4000 kJ/(mol nm^2) or if k_{dc} goes to zero. Each of the four trajectories has one or two NOE violations of about 0.1 nm at k_{dc} = 0 kJ/(mol nm^2). Similar to the vacuum RMD results at k_{dc} = 0 and 4000 kJ/(mol nm^2), all four trajectories have NOE violations greater than or equal to 0.060 nm for the Trp^9-(HE3)-Trp^9(HA) distance. Similar to the vacuum RMD results at k_{dc} = 0 kJ/(mol nm^2), the DG3 and DG4 trajectories exhibit violations on the order of 0.1 nm for the Tyr^2(H)-Ser^3(H) distance. For both the vacuum and solvent RMD results, the DG4 trajectory has a large NOE violation for Trp^9(HD1)-Trp^9(HA) at k_{dc} = 0 and 4000 kJ/(mol nm^2). Although Tables 6 and 7 show several common proton pairs with large NOE violations, there are also differences between the tables. The DG2 trajectory shows a large violation at k_{dc} = 4000 and 0 kJ/(mol nm^2) for Ser^3(H)-Tyr^2(HA) which appears in the solvent but not in the vacuum simulation. Comparison of Tables 6 and 7 shows that inclusion of explicit solvent in the simulation does not seem to lead to a particularly better fit of the structures to the NOE distance constraints.

The situation is somewhat different when comparing the vacuum and solvent TARMD results to their vacuum and solvent RMD counterparts. Table 8, presenting the vacuum TARMD results, shows the same trend as the vacuum and solvent RMD results above, in that the Trp^9-(HE3)-Trp^9(HA) distance is greater than or equal to 0.060 nm for the DG1, DG3, and DG4 trajectories at k_{dc} = 0

kJ/(mol nm^2). In addition, the DG1 and DG2 trajectories show large violations, on the order of 0.1 nm, for Trp^9-(H)-Arg^8(HA). And, as above, none of the four trajectories satisfies the distance constraints if the restraining potential goes to zero. What is strikingly different from the RMD results is that, for large values of k_{dc}, the four TARMD vacuum trajectories satisfy the distance constraints. At $k_{dc} = 4000$ and 2000 kJ/(mol nm^2), all four trajectories satisfy the criteria. By contrast, the trajectories of the RMD vacuum simulations show more total and larger individual violations than do those of the TARMD method. This indicates that the TARMD method allows for a better fit to the experimental NOE data at the highest restraining forces for both the vacuum and solvent simulations.

The same result is seen in comparing the solvent TARMD results of Table 9 to the solvent RMD results of Table 7. Table 9 shows that all four distance-geometry trajectories satisfy the distance constraints at $k_{dc} = 4000$ and 2000 kJ/(mol nm^2). As with the vacuum TARMD simulation, the size and number of large violations increases if k_{dc} goes to zero. By contrast, the vacuum and solvent RMD results show that the number and size of large NOE violations are independent of k_{dc}. The results of Table 9 support the view that the TARMD method allows for a better fit of the molecular structure to the NOE data than the RMD method. Moreover, the fact that the number and size of violations increase if k_{dc} goes to zero indicates that the force field alone is unable to constrain the molecule to fit the experimental data.

In terms of common NOE violations, the DG1, DG3, and DG4 trajectories in Table 9 all show large violations for Trp^9(HE3)-Trp^9(HA) at $k_{dc} = 0$ kJ/(mol nm^2). This is similar to the results of the solvent RMD simulations of Table 7. Similarly, both methods give large violations for Tyr^2(H)-Ser^3(H) for the DG1, DG3 and DG4 trajectories at $k_{dc} = 0$ kJ/(mol nm^2).

Comparison of the solvent TARMD results of Table 9 to the vacuum TARMD results of Table 8 shows that the solvent TARMD method does not give a significantly better fit to the NOE data than the vacuum TARMD method. This behavior was also noted in the comparison

TABLE 7
NOE VIOLATIONS IN RMD SOLVENT SIMULATIONS

Structure/NOE	k_{dc} (kJ/(mol nm^2))					
	4000 (10–60)[a]	2000 (60–70)	1000 (70–80)	500 (80–90)	250 (90–100)	0 (100–150)
DG1						
Tyr^2(H)-Ser^3(H)	0.128	0.132	0.110	0.111	0.132	0.135
Ser^3(H)-Met^4(H)	–	–	–	–	0.071	–
Trp^9(HE3)-Trp^9(HA)	0.157	0.153	0.123	0.170	0.176	0.180
Trp^9(HD1)-Trp^9(HA)	–	–	–	–	0.066–	0.069-
Total violations[b]	5/9	6/6	6/7	8/7	8/6	6/8
DG2						
Tyr^2(H)-Ser^3(H)	–	–	–	0.078	–	–
Ser^3(H)-Met^4(H)	–	–	–	–	–	0.079-
Tyr^2(H)-Ser^1(HA)	0.077	0.071	–	–	0.072	0.074
Ser^3(H)-Tyr^2(HA)	0.120	0.125	0.124	0.125	0.123	0.122
Arg^8(H)-Arg^8(HG)	0.064–	–	0.061–	0.061–	–	–
Trp^9(HE3)-Trp^9(HA)	0.144	0.099	0.133	0.129	0.144	0.153
Total violations	5/7	6/7	5/8	6/9	6/8	7/10
DG3						
Tyr^2(H)-Ser^3(H)	–	0.118	0.107	0.126	0.122	0.116
Met^4(H)-Met^4(HB)	–	0.074–	0.076–	0.068	0.067–	–
Trp^9(HE3)-Trp^9(HA)	0.149	0.168	0.153	0.167	0.181	0.174
Total violations	6/9	5/8	6/7	5/7	5/10	6/9
DG4						
Tyr^2(H)-Ser^3(H)	0.071	0.089	0.075	0.119	0.130	0.124
Ser^3(H)-Met^4(H)	–	0.070–	–	0.072–	0.085–	–
Arg^8(H)-Arg^8(HG)	–	–	0.076–	0.080–	0.070–	–
Trp^9(HE3)-Trp^9(HA)	0.139	0.116	0.084	0.077	0.084	0.088
Trp^9(HD1)-Trp^9(HA)	0.065	0.081	0.103	0.107	0.105	0.098
Total violations	5/9	5/8	6/8	5/9	4/7	5/6

Distances in nm; lower bound violations are indicated by a '–' following the number, numbers without this indication are upper bound violations.
[a] Time interval (ps).
[b] Number of upper bound violations/number of lower bound violations.

TABLE 8
NOE VIOLATIONS IN TARMD VACUUM SIMULATIONS

Structure/NOE[a]	k_{dc} (kJ/(mol nm^2))					
	4000 (20–100)[b]	2000 (100–120)	1000 (120–140)	500 (140–160)	250 (160–180)	0 (180–260)
DG1						
Glu^5(H)-Met^4(HA)	–	–	–	–	–	0.067
Arg^8(H)-Arg^8(HA)	–	–	–	–	–	–
Trp^9(H)-Arg^8(HA)	–	–	–	–	0.098	0.099
Trp^9(HE3)-Trp^9(HA)	–	–	–	–	–	0.149
Total violations[c]	3/4	2/6	4/7	5/6	8/6	10/10
DG2						
Tyr^2(H)-Ser^3(H)	–	–	–	0.067	–	–
Glu^5(H)-Met^4(HA)	–	–	–	–	0.080	0.072
Trp^9(H)-Arg^8(HA)	–	–	–	0.099	0.097	0.096
Met^4(H)-Met^4(qb2)	–	–	–	–	0.075–	–
Trp^9(HE3)-Trp^9(HA)	–	–	–	–	–	–
Total violations	6/3	5/6	5/4	7/5	9/4	10/4
DG3						
Ser^3(H)-Tyr^2(HA)	–	–	–	–	–	0.067
Glu^5(H)-Met^4(HA)	–	–	–	0.062	0.083	0.087
Trp^9(HE3)-Trp^9(HA)	–	–	0.087	–	–	0.066
Total violations	2/3	5/5	5/5	9/5	5/4	9/6
DG4						
Tyr^2(H)-Ser^3(H)	–	–	0.085	0.079	0.068	–
Ser^3(H)-Tyr^2(HA)	–	–	–	0.096	–	–
Met^4(H)-Met^4(qg2)	–	–	–	–	0.092–	–
Trp^9(HE3)-Trp^9(HA)	–	–	–	–	0.063	0.153
Total violations	3/3	4/5	5/4	7/6	5/6	4/7

Distances in nm; lower bound violations are indicated by a '–' following the number, numbers without this indication are upper bound violations.
[a] qb2 or qg2 indicates the average position of the two protons on CB or CG, respectively.
[b] Time interval (ps).
[c] Number of upper bound violations/number of lower bound violations.

of the solvent and vacuum RMD results. This indicates that the inclusion of explicit solvent may not be particularly useful in improving the fit to the distance constraints in either the TARMD or the RMD simulations.

The major trend in all four tables is the large size of the Trp^9(HE3)-Trp^9(HA) distance for almost all of the structures at $k_{dc} = 0$. In many cases, the Tyr^2(H)-Ser^3(H) distance is also large. None of the original distance-geometry starting structures (Table 5) exhibited these trends. Moreover, NOE violations invariably appear for proton pairs that are associated with torsional angles that have most of their conformational space excluded (Table 1). This indicates that, as the structures were subjected to the force field, they were unable to remain in the artificial conformers which satisfied the distance constraints. This seems to implicate inadequacies in the force field, such as the lack of inclusion of the effects of polarization, among other factors.

Conformational transitions

Conformational transitions in the macrocycle, defined as the change from trans- to cis-orientation in the backbone torsional angle of the peptide bond, were monitored by plotting the change in ω (CA-C-N'-CA') versus time. Of the four trajectories, only the vacuum TARMD simulation exhibited any conformational transitions. This is not surprising, since conformational transitions in MD simulations with explicit water molecules usually appear only in long (1 ns) simulations, as for example in the case of B-DNA [105]. These transitions occurred for ω of Met^4 in DG3 (Fig. 3a), His^6 in DG3 (Fig. 3b), and Arg^8 in DG2 (Fig. 3c). Since the vacuum TARMD method should allow the greatest flexibility of the macrocycle in fitting to the NOE constraints over time, these trends are not unexpected. It is interesting to note that the conformational transitions in Figs. 3a and 3b take place during the first 100 ps of the trajectory, when $k_{dc} = 4000$ kJ/(mol nm^2), whereas the transition in Fig. 3c occurs during the interval 120–140 ps, when $k_{dc} = 1000$ kJ/(mol nm^2). No transitions were found with the restraining force turned off.

Backbone torsional angles

Figure 4 depicts histogram distributions of the stan-

TABLE 9
NOE VIOLATIONS IN TARMD SOLVENT SIMULATIONS

Structure/NOE[a]	k_{dc} (kJ/(mol nm^2))					
	4000 (20–100)[b]	2000 (100–120)	1000 (120–140)	500 (140–160)	250 (160–180)	0 (180–260)
DG1						
Tyr^2(H)-Ser^3(H)	–	–	0.120	0.126	0.122	0.126
Trp^9(HE3)-Trp^9(HA)	–	–	–	0.103	0.129	0.145
Total violations[c]	7/6	7/5	8/6	7/7	7/7	5/9
DG2						
Tyr^2(H)-Ser^3(H)	–	–	0.074	0.061	0.061	0.087
Ser^3(H)-Met^4(H)	–	–	0.061	0.068	–	0.062
Met^4(H)-Met^4(qb2)	–	–	–	–	–	0.060
Trp^9(HD1)-Trp^9(HA)	–	–	–	0.073	0.077	0.081
Total violations	3/6	4/6	4/5	5/9	5/8	4/8
DG3						
Tyr^2(H)-Ser^3(H)	–	–	0.094	0.108	0.098	0.100
Ser^3(H)-Met^4(H)	–	–	0.067	–	0.061	0.077
Arg^8(H)-Arg^8(qg2)	–	–	–	–	0.067–	–
Trp^9(HE3)-Trp^9(HA)	–	–	–	–	0.096	0.145
Total violations	6/8	7/7	6/5	5/6	4/6	5/9
DG4						
Tyr^2(H)-Ser^3(H)	–	–	0.063	0.080	–	0.127
Met^4(H)-Met^4(HG)	–	–	–	–	0.114–	0.109–
Trp^9(HE3)-Trp^9(HA)	–	–	–	–	–	0.110
Total violations	4/8	4/10	3/11	5/6	5/8	4/7

Distances in nm; lower bound violations are indicated by a '–' following the number, numbers without this indication are upper bound violations.
[a] qb2 or qg2 indicates the average position of the two protons on CB or CG, respectively.
[b] Time interval (ps).
[c] Number of upper bound violations/number of lower bound violations.

dard deviations of all of the ϕ (N-CA-C-N') and ψ (C-N-CA-C') backbone torsional angles. Each histogram is a composite of the standard deviations of both backbone torsional angles for all 10 amino acid residues for the four distance-geometry structure simulations for k_{dc}=4000 kJ/(mol nm^2) and k_{dc} = 0 kJ/(mol nm^2). This results in a total of 80 data points for each histogram. Figure 4a shows that the distribution for k_{dc} = 4000 kJ/(mol nm^2) in the vacuum RMD simulations exhibits several large values for the standard deviation which are not present when the restraining force is removed. It is clearly evident from Fig. 4b that the trajectories in the vacuum TARMD simulations exhibit much more variability when the restraining force is on than when k_{dc} = 0 kJ/(mol nm^2). This type of variability has been previously noted in other systems [106]. This distribution is, by far, the most anomalous of the four presented in Fig. 4.

Figure 4c gives the distribution for the solvated RMD simulations. It shows that the standard deviations for k_{dc} = 4000 kJ/(mol nm^2) and k_{dc} = 0 kJ/(mol nm^2) are almost identical. This case is the only one of the four which does not have a distribution shifted to the right when k_{dc} =

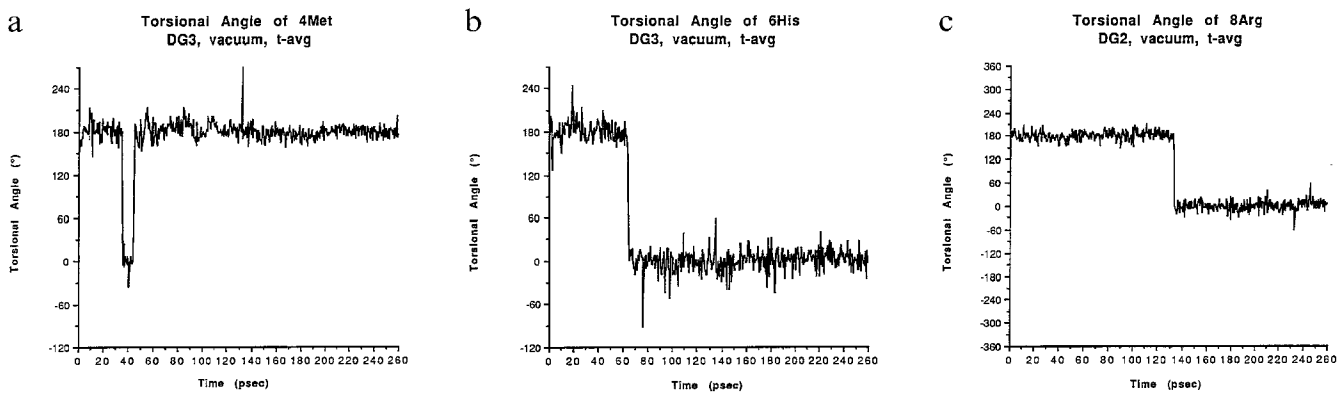

Fig. 3. Torsional angle conformational changes for the vacuum TARMD trajectories. (a) Met^4 of DG3; (b) His^6 of DG3; (c) Arg^8 of DG2.

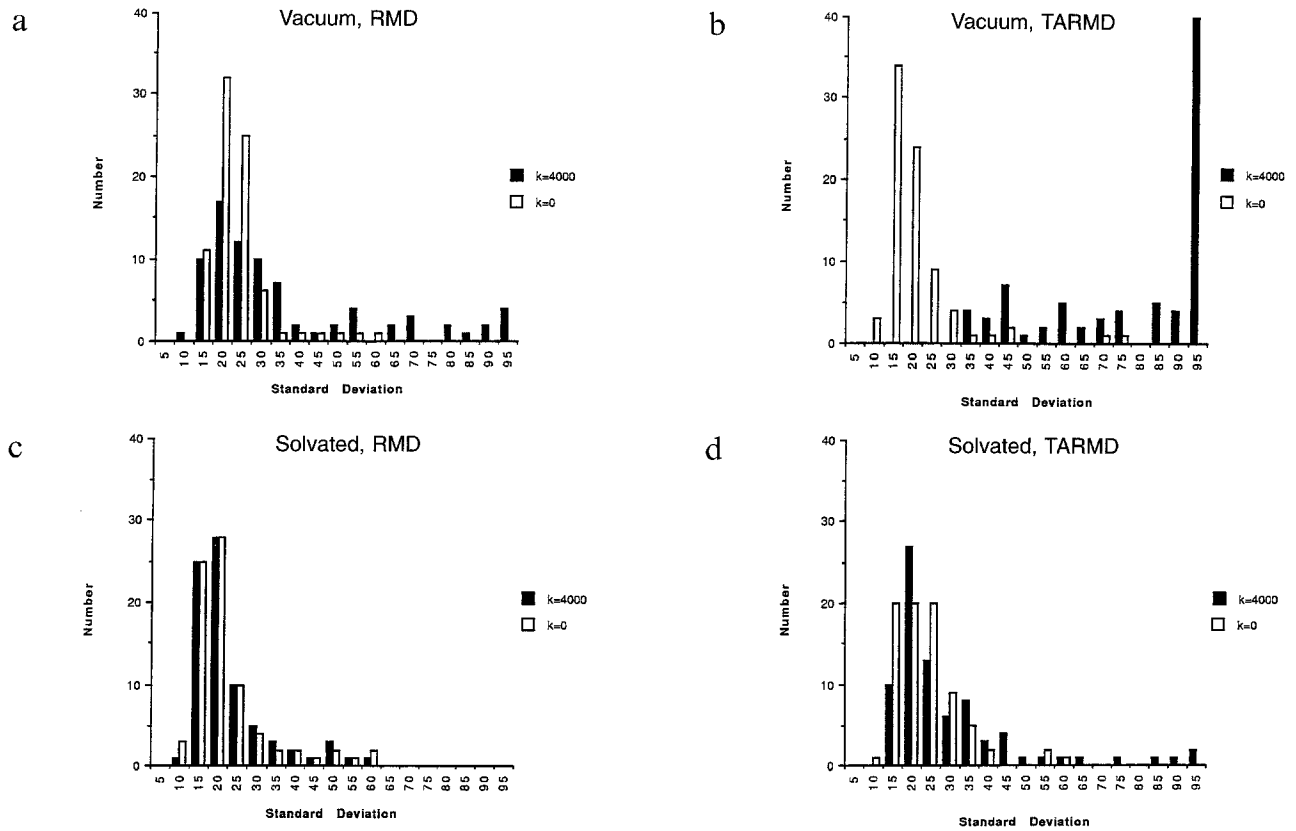

Fig. 4. Histogram distributions of the standard deviations of the ϕ (N-CA-C-N) and ψ (C-N-CA-C) backbone torsional angles in 5° increments for all the simulations. The vertical axis gives the number of ϕ and ψ angles within a particular standard deviation. The horizontal axis gives the range of standard deviations, with the first block being 0–5, etc. Values in block 95 are for all standard deviations greater than 90. (a) Vacuum RMD; (b) vacuum TARMD; (c) solvent RMD; (d) solvent TARMD.

4000 kJ/(mol nm^2). Figure 4d shows the distributions for the solvated TARMD simulations. Like the vacuum TARMD case, several large standard deviations, indicative of conformational variability, are found when k_{dc} = 4000 kJ/(mol nm^2).

Comparison of the vacuum and solvent simulations for the same value of the restraining force constant shows, in general, that solvent molecules dampen the motion of the cyclic peptide, as evidenced by a shift in the distributions to the left. This is also seen in the rms superpositions below. Besides, as expected, distributions of the vacuum and solvent simulations with both methods are similar when the restraining force is turned off. They are not identical, because the starting structures, velocities, and forces for the trajectory intervals used were not identical. Finally, in comparing the RMD and TARMD methods fort k_{dc} = 4000 kJ/(mol nm^2) to k_{dc}=0 kJ/(mol nm^2), both the vacuum and solvent simulations show increased variability, as evidenced by a shift to the right in the histogram (Fig. 4).

Rms superposition

As seen from rms superposition of the peptide-backbone C^{α}s of each conformer, in a particular k_{dc} interval of the trajectory onto the first structure in that interval (not shown), the NOE data are sufficient to define a somewhat similar backbone conformation for all the structures, but not to define the positions of the side chains, which show considerable motion. An example of this is shown in Fig. 5, which gives the results of rms superpositions of 5-ps 'snapshots' along the TARMD vacuum and solvent trajectories for DG1. For the vacuum case, comparison of Figs. 5a and 5b shows that the structures are more similar at k_{dc}=0 kJ/(mol nm^2) than at k_{dc}=4000 kJ/(mol nm^2). In both cases, the side-chain positions vary considerably, with the largest variability being at k_{dc} = 4000 kJ/(mol nm^2). For the solvent case, there is less of a difference between the results with the two different restraining potentials. However, comparison of the vacuum and solvent TARMD results shows that the solvent clearly dampens the motion of the side chains. For comparison of the RMD and TARMD results, Fig. 5e also gives the superpositions of 5-ps 'snapshots' for the RMD solvent trajectory at k_{dc}=4000 kJ/(mol nm^2) for DG1. Comparison to Fig. 5c shows that there is less fluctuation in the backbone and side chains with the RMD method.

The most striking result of these superpositions, regardless of the fluctuations in the positions of the side chains, is that the Ser^1 or Ser^3 and His^6 components of the catalytic triad, located across the macrocycle from each other, are simply too far apart for proton transfer.

In no case does the macrocycle fold so as to bring them closer together. In addition, as noted above, the Glu^5 and His^6 residues, although located next to each other, are unable to attain the hydrogen-bonding distance seen in the X-ray structure of chymotrypsin [107] and in Cram's spherand mimics [19,37] for the carboxylate and imidazole moieties, because their side chains point away from each other.

Table 10 lists average rms deviations of C^α superpositions to test for convergence of the four distance-geometry trajectories to a single structure and to test the effect of the NOE restraining force on conformational variability. The large changes seen in the convergence tests in Table 10 clearly indicate that the simulations do not converge to a common structure. The results of the TARMD simulations run with a 5-ps memory length (given in parentheses in Table 10) show slightly smaller rms values (0.009–0.096 nm) than the simulations with a memory length of 2.5 ps, but in general these results support the conclusion that the simulations do not converge to a common structure. Table 11 reports the rms results for the 16 additional distance-geometry structures and supports the above conclusion. Tables 10 and 11 show that there is variability in the vacuum structures with both the RMD and TARMD methods. A striking difference is found with the TARMD method. Again, the results of the TARMD simulation run with a 5-ps memory length, given in parentheses in Table 10, show slightly smaller rms values (0.013–0.051 nm) than the simulations with a memory length of 2.5 ps. The TARMD simulations with a 5-ps memory length still show significant conformational variability in the cyclic peptide. The data also indicate that the variabilities in the vacuum simulations are about twice those of the solvent simulations. Furthermore, as expected, the data show similar changes in all simulations when the restraining force is turned off.

Catalytic triad

An important feature of any potential serine protease mimic is the relative orientation of the functional carboxylate, imidazole, and hydroxyl moieties of the catalytic triad. The hydrogen-bonding distances between proton donors and acceptors on His^6 and Ser^1 or Ser^3 and on His^6 and Glu^5 were monitored for each of the trajectories. Only a few of the structures showed hydrogen-bonding patterns which persisted over 50% of the trajectory and these varied with the value of k_{dc}. The following discussion compares the findings for only $k_{dc} = 4000$ or 0 kJ/

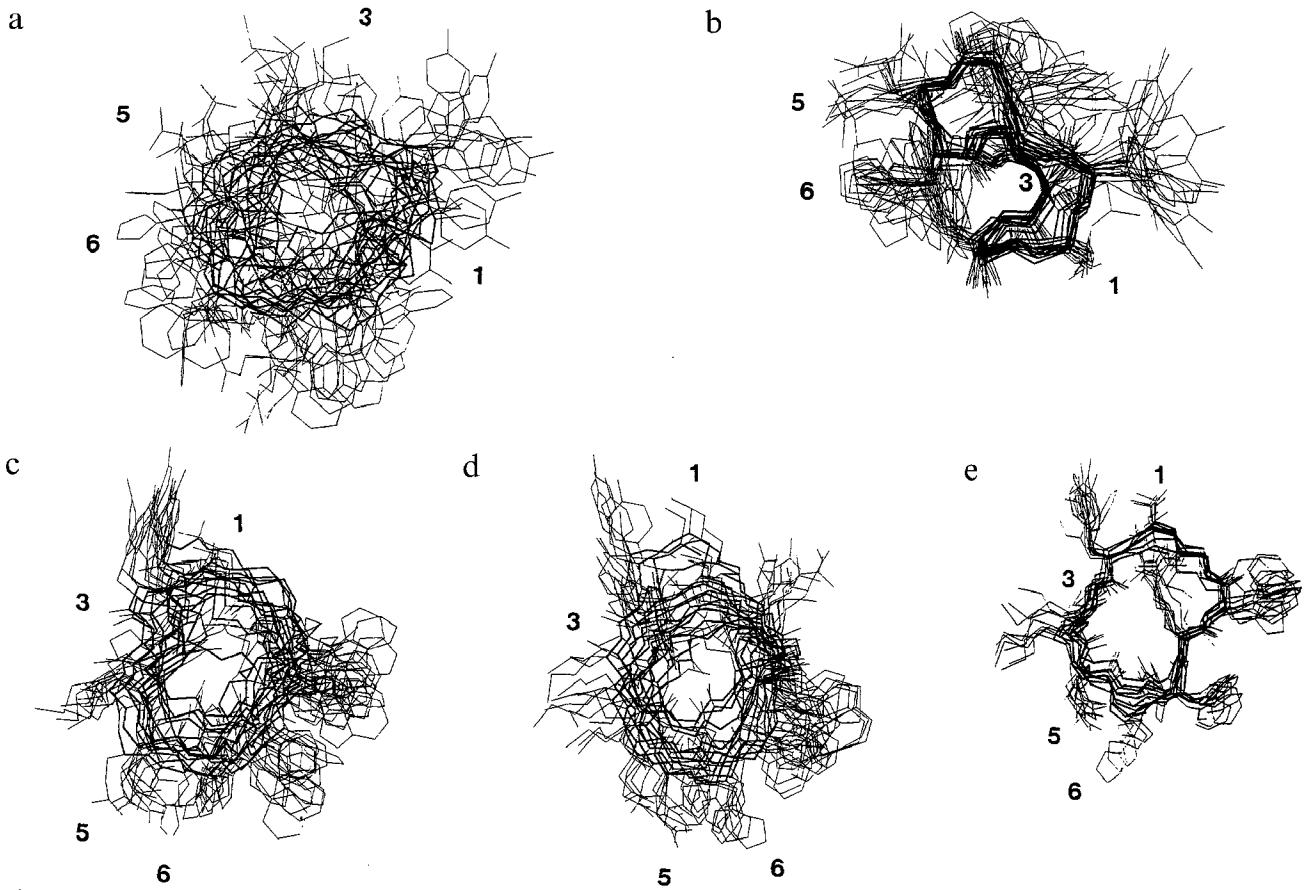

Fig. 5. Rms structural superpositions of successive conformations in the DG1 TARMD and RMD trajectories. The C^α backbones are shown as thick lines. (a) TARMD, vacuum, $k_{dc} = 4000$ kJ/(mol nm^2); (b) TARMD, vacuum, $k_{dc} = 0$ kJ/(mol nm^2); (c) TARMD, solvent, $k_{dc} = 4000$ kJ/(mol nm^2); (d) TARMD, solvent, $k_{dc} = 0$ kJ/(mol nm^2); (e) RMD, solvent, $k_{dc} = 4000$ kJ/(mol nm^2).

TABLE 10
RMS SUPERPOSITIONING FOR TRAJECTORIES: TEST FOR CONVERGENCE AND CONFORMATIONAL VARIABILITY OF STRUCTURES DG1–DG4[a]

	Convergence				Conformational variability			
	Vacuum		Solvent		Vacuum		Solvent	
	RMD[b] (nm)	TARMD (nm)	RMD (nm)	TARMD (nm)	RMD (nm)	TARMD (nm)	RMD (nm)	TARMD (nm)
DG1	0.102	0.287 (0.256)[c]	1.41	0.114	0.102	0.287 (0.244)	0.141	0.114
	0.247	0.329	2.44	0.195	0.248	0.112	0.052	0.091
DG2	0.320	0.361 (0.265)	2.65	0.285	0.197	0.277 (0.264)	0.070	0.127
	0.356	0.285	2.39	0.316	0.114	0.056	0.083	0.060
DG3	0.379	0.266 (0.242)	3.65	0.335	0.127	0.282 (0.231)	0.091	0.069
	0.392	0.446	3.85	0.321	0.123	0.112	0.040	0.110
DG4	0.403	0.271 (0.262)	2.77	0.313	0.249	0.307 (0.261)	0.073	0.090
	0.422	0.432	2.76	0.288	0.195	0.161	0.094	0.113

[a] See Results (Trajectories) section for description of rms procedure for each type of test.
[b] For each structure the upper (lower) row gives results for $k_{dc} = 4000$ (0) kJ/(mol nm^2).
[c] Numbers in parentheses are from the simulation with a memory length of 5 ps.

(mol nm^2). For the vacuum RMD trajectories, only DG2 and DG3 exhibited hydrogen bonds for 50–60% of the time between the side chain of His^6 and the backbone carbonyl of Glu^5 at k_{dc} equal to 4000 kJ/(mol nm^2). Only for DG2 did this phenomenon persist at $k_{dc} = 0$ kJ/(mol nm^2). For the TARMD simulations with a memory length of 5 ps at k_{dc} equal to 4000 kJ/(mol nm^2), no structures showed hydrogen-bonding patterns which persisted over 50% of the trajectory. DG1 showed hydrogen bonding between His^6 and Glu^5 for 17% of the time, while DG3 exhibited hydrogen bonds between these residues for 25% of the time. Hydrogen bonding between Ser^1 or Ser^3 and His^6 was negligible. For the TARMD simulations of the 16 additional starting structures, all of the structures showed some hydrogen bonding between His^6 and Glu^5, with only DG3d (at 55%) exhibiting hydrogen bonding for more than 50% of the time. DG2c exhibited hydrogen bonding between Ser^1 and His^6 for 10% of the time, while DG3b exhibited hydrogen bonding between Ser^3 and His^6 for 17% of the time.

For the solvated RMD trajectories, DG1 exhibited hydrogen bonds between the backbone amino group of His^6 and the side chain of Glu^5 for 60–80% of the time at $k_{dc} = 4000$ kJ/(mol nm^2). This increased to almost 100% at $k_{dc} = 0$ kJ/(mol nm^2), but involved side chains of both the charged amino acids. DG3 exhibited these hydrogen bonds only at $k_{dc} = 0$ kJ/(mol nm^2). For the vacuum TARMD and solvated TARMD, hydrogen bonds were found between the backbone of His^6 and Glu^5 only at $k_{dc} = 0$ kJ/(mol nm^2) for DG2 (54%, vacuum TARMD) and the side chains of His^6 and Glu^5 for DG1 (71%, solvated TARMD). In addition, only DG2 of the vacuum TARMD showed hydrogen bonds between His^6 and Ser^3 for 53% of the time at $k_{dc} = 0$ kJ/(mol nm^2). This seems to indicate that, in general, the macrocycle is too flexible to hold the 'catalytic triad' in a geometric relationship similar to that found in the serine proteases.

Substrate modeling

Figure 6 shows the size of the substrate relative to the $cACTH_{1-10}$ cavity. The substrate is about 1.0 nm in length, while the diameter of the macrocycle is about 1.2–1.5 nm. The cavity clearly cannot provide the secondary binding sites of the chymotrypsin active site [108].

Catalytic activity

A slight increase in the hydrolysis rate of the substrate

TABLE 11
RMS SUPERPOSITIONING FOR TRAJECTORIES: TEST FOR CONVERGENCE AND CONFORMATIONAL VARIABILITY OF 16 ADDITIONAL DISTANCE-GEOMETRY STRUCTURES[a]

Structure[b]	Convergence rms (nm)	Conformational variability rms (nm)
DG1a	0.252	0.252
DG1b	0.247	0.237
DG2a	0.239	0.229
DG2b	0.234	0.228
DG3a	0.249	0.249
DG3b	0.258	0.260
DG4a	0.249	0.246
DG4b	0.245	0.240
DG1c	0.242	0.238
DG1d	0.228	0.219
DG2c	0.246	0.230
DG2d	0.233	0.224
DG3c	0.257	0.229
DG3d	0.232	0.246
DG4c	0.266	0.259
DG4d	0.234	0.233

[a] See Results (Trajectories) section for description of rms procedure for each type of test.
[b] As described in the text, DG1a and DG1b are the two lowest energy-minimized structures of the eight snapshots from the simulation of DG1 using a 2.5-ps memory length; DG1c and DG1d are the two lowest energy-minimized structures of the eight snapshots from the simulation of DG1 using a 5-ps memory length, etc.

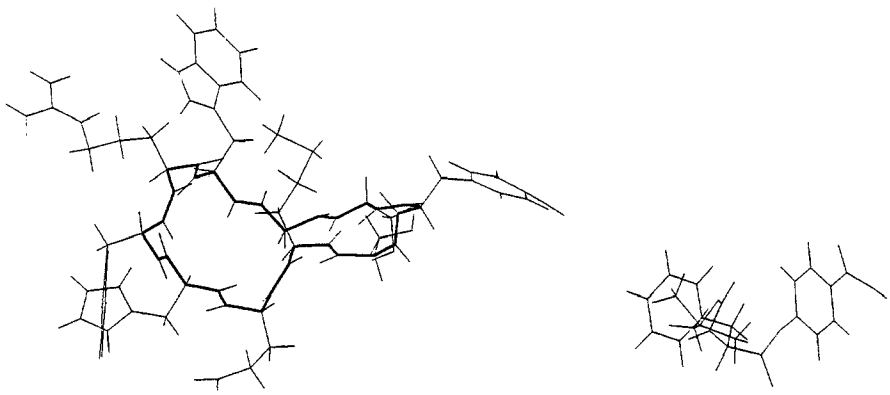

Fig. 6. Boc-Phe-ONp and $cACTH_{1-10}$ (DG1 starting structure).

Boc-Phe-ONp was observed in the presence of cyclic form **IV** of $ACTH_{1-10}$ ($(3.5 \pm 0.3) \times 10^{-7}$ mol/min; n = 5) but no statistically significant increase was observed in the presence of linear $ACTH_{1-10}$ **V** ($(3.2 \pm 0.3) \times 10^{-7}$ mol/min; n = 5) compared to the control ($(2.7 \pm 0.22) \times 10^{-7}$ mol/min; n = 8), where n is the number of measurements. Boc-D-Phe-ONp was hydrolyzed at the same rate as the L-isomer, in contrast to α-chymotrypsin which favors the L-isomer. The small (30%) increase in the hydrolysis rate in the presence of $cACTH_{1-10}$ compared to solvent supports the findings of the molecular dynamics simulations and the NMR study, which seem to indicate that $cACTH_{1-10}$ is too flexible to hold the catalytic triad in place.

Discussion

The goals of this work have been to determine the solution structure of $cACTH_{1-10}$ by the combined use of NMR spectroscopy and RMD simulations and to evaluate four different simulation methods for their ability to fit a structure to the NMR data. These, in turn, allowed an assessment of their utility in computer-aided molecular design studies and an evaluation of the molecule as a potential mimic of the serine protease, chymotrypsin. In comparing the four simulation models, the major findings are:

(1) the TARMD method allows for a better fit of the molecular structure to the NOE data at large values of k_{dc} in both the vacuum and solvent cases. Analysis of the backbone torsional angles indicates that the TARMD method (in both vacuum and solvent) allows for structures with more conformational variability than does the RMD method;

(2) use of solvent is not an advantage in obtaining a better fit to the distance constraints in either the RMD or TARMD methods. Inclusion of the solvent is found, however, to clearly dampen some of the flexibility of the macrocycle, since: (i) conformational transitions were observed only in the vacuum TARMD trajectory; (ii) the rms superpositions give larger values for the vacuum simulations; and (iii) the standard deviations of the backbone torsional angles are greater in the vacuum simulations;

(3) the increase in the number and size of the NOE violations if k_{dc} goes to zero occurs in both the vacuum and solvent RMD and TARMD simulations, indicating possible inadequacies in the GROMOS force field;

(4) imposition of the largest restraining force constant, $k_{dc} = 4000$ kJ/(mol nm^2), results in more conformational variability of backbone torsional angles compared to the results at $k_{dc} = 0$ kJ/(mol nm^2);

(5) most violations are found in those NOEs where the systematic conformational search indicated that the excluded space is on the order of 80–90%;

(6) increasing the size of the memory length from 2.5 to 5 ps and increasing the sample size by 16 additional starting structures did not add to the above findings.

The improved sampling properties of the vacuum TARMD method compared to the RMD method have been noted by others and should prove to be more efficacious in future modeling studies. Brunne and Liebfritz [86] showed that only with the vacuum TARMD method could conformational transitions be observed in Boc-Ala-Aib-Ala-OMe. Pearlman and Kollman [109] showed that the TARMD method gave a much better picture of the conformational flexibility and the fine conformational detail for the *Eco*RI restriction site DNA hexamer $d(GAATTC)_2$. Similar results were obtained for the FK506 macrocycle [110] and the adenosine nucleotide [106]. In general agreement with the results obtained here, Pearlman [110] has noted that rms fluctuations are relatively insensitive to the value of k_{dc} for RMD vacuum simulations, but increase with increasing k_{dc} for TARMD vacuum simulations. Kessler and co-workers [83,84] found that the vacuum TARMD method gave important information about conformational transitions for two cyclic peptides. The vacuum TARMD study by Torda et al. [80] on tendamistat showed that the technique allowed greater flexibility to the molecule and gave a better estimate of the conformational space occupied by the molecule in

solution. Schmitz et al. [111] found more realistic conformational sampling of intranucleotide geometries with TARMD than with RMD for the DNA fragment d(GTATAAGT)·d(CATATTAC).

Care must be taken, however, in interpretation of conformational changes found in vacuum simulations. It is well known that vacuum simulations of proteins with charged residues lead to unphysical results. In this work, the RT37C GROMOS parameter set, which compensates for the lack of solvent screening in vacuum calculations by using neutral amino acid residues, was used to avoid such problems in the RMD and TARMD vacuum simulations. Yet, for the vacuum TARMD simulations, three cases of the peptide-backbone torsional angle interconversion from trans- to cis-orientation were observed. These results could very well be an artifact of the methodology and the incorporation of exogenous forces based on the NMR data into the force field. The combined effect of these forces could be the reason why the 73-kJ/mol GROMOS peptide torsional barrier could be overcome.

However, the major problem in determining the solution structure of $cACTH_{1-10}$ lies in the lack of long-range NOEs. Since all the experimental NOEs are between protons within the same amino acid residue or between protons on neighboring residues, the available data are simply insufficient to determine a definitive conformation or a time-averaged set of conformations. This, of course, is due to the fact that the cyclic decapeptide is very flexible. However, the large flexibility and small size of $cACTH_{1-10}$ may explain its poor activity as an enzyme mimic, since it is unable to appreciably bind, encapsulate, desolvate, or orient the relatively large substrate in a manner necessary for productive binding and catalysis.

The dimensions and components of the active site are also important features to be considered in the design of an enzyme mimic. For example, in their four-α-helical-bundle mimic of chymotrypsin, Hahn et al. [26] included not only the catalytic triad, but also the necessary oxyanion hole and substrate-binding pocket for acetyltyrosine ethyl ester. These features are missing in $cACTH_{1-10}$. In their 29-residue cyclic peptide mimic (TrPepz) of chymotrypsin, Atassi and Manshouri [28] took 19 residues of the active site of chymotrypsin and linked them by glycine spacer groups. However, ^1H NMR [30] and molecular dynamics simulations [32] have shown that the structure of this cyclic peptide is disordered. This is due to the small and flexible glycine residues, which Matthews et al. [29] have identified as the source of flexibility in the cyclic peptide. Corey and Phillips [31] have shown that TrPepz exhibits no esterase or amidase activity, which supports the idea that the cyclic peptide is too flexible to hold the catalytic triad in place. The $cACTH_{1-10}$ macrocycle, while containing the functional groups of the chymotrypsin catalytic triad, has been shown here also to be too flexible to hold the catalytic triad in place.

In terms of the design of a functioning enzyme mimic, not only the distance, but also the orientation of the residues is important to catalysis. For example, Gandour [112] has noted that the syn lone pair of a carboxylate is about 104 times more basic than the anti lone pair, and that the active sites of enzymes are designed so as to exploit that difference. So, for optimal reactivity, a model system should be designed so as to force an electrophilic substrate to approach the syn rather than the anti lone pair. Rebek [113] has explored these design principles in a series of molecular clefts in which carboxylate moieties converge upon a binding cavity. Li and Houk [114] have studied the source of the difference in the reactivity of the syn versus anti lone pairs by an ab initio quantum-mechanical study of a model system, the deprotonation of acetaldehyde by formate anion. In addition, from computer graphics inspection of the X-ray structure of chymotrypsin, Rebek [115] has proposed that ring flipping of the imidazole of the His^{57} side chain may be an important feature of the active site in that it would allow for proton transfer in a variety of directions.

However, the molecular modeler may be allowed some degree of flexibility in trying to reproduce the enzyme's active site using an alternative molecular scaffolding in an enzyme mimic. Corey et al. [116,117] have investigated the minimum requirements for peptide hydrolysis by site-specific mutagenesis of the catalytic triad of trypsin. They found that of the three components of the catalytic triad only serine is essential for the cleavage of unactivated amide bonds by trypsin, and that the presence of an adjacent basic residue, lysine or histidine, can improve the rate of catalysis. Therefore they recommended the initial design of a protease mimic which consists of an oxyanion hole, transition-state stabilization by substrate binding, and a strategically placed nucleophile (not necessarily serine). They also showed that part of the effect of the function of Asp^{102} in catalysis could be reproduced by the replacement of the neighboring Ser^{214} by an aspartic or glutamic acid [116].

The preliminary studies presented in this paper provide a starting point for the redesign of a cyclic peptide enzyme mimic. The results indicate that the poor rate of hydrolysis exhibited by $cACTH_{1-10}$ may be attributed to the small size and flexibility of the cyclic decapeptide and to the poor spatial relationships between the catalytic components. These studies and those of others [13,17,26, 28,30,31,118] highlight the important features to be included in an improved molecular design [29]: (i) a catalytic triad held in place by a rigid molecular architecture; and (ii) sufficient residues to provide an oxyanion hole and a binding pocket, which can align the scissile peptide bond of the substrate in proper orientation to the catalytic triad and oxyanion hole. Whether these features can be reproduced by a cyclic peptide or by a cyclic peptide/heterocycle hybrid remains to be seen.

Acknowledgements

This work was funded in part by a grant to C.A.V. from the U.S.-Western Europe Cooperative Science Program of the National Science Foundation. C.A.V. and R.A.B. would like to thank A. Torda and R. Brunne for help with implementation of the TARMD routines of GROMOS. C.A.V. would like to thank W.F. van Gunsteren for the GROMOS program and for hospitality during her sabbatical stay at the University of Groningen. J.L.F. would like to thank Mrs. A.M. Brebbia for expert technical assistance. Thanks are due to C. Lindblah, laboratory of K. Mosbach, University of Lund, Sweden, for performing some of the biochemical measurements and to R.M. Scheek, University of Groningen, for performing the distance-geometry calculations and assistance with the NMR measurements.

References

1 Torda, A.E. and Van Gunsteren, W.F., In Lipkowitz, K.B. and Boyd, D.B. (Eds.), Reviews in Computational Chemistry, Vol. III, VCH, New York, NY, 1992, p. 143.
2 Breslow, R., Czarniecki, M.F., Emert, J. and Hamaguchi, H., J. Am. Chem. Soc., 102 (1980) 762.
3 Trainor, G.L. and Breslow, R., J. Am. Chem. Soc., 103 (1981) 154.
4 Breslow, R., Trainor, G. and Ueno, A., J. Am. Chem. Soc., 105 (1983) 2739.
5 Breslow, R., Czarnick, A.W., Lauer, M., Leppkes, R., Winkler, J. and Zimmerman, S., J. Am. Chem. Soc., 108 (1986) 1969.
6 Thiem, H.-J., Brandl, M. and Breslow, R., J. Am. Chem. Soc., 110 (1988) 8612.
7 Breslow, R. and Chung, S., Tetrahedron Lett., 31 (1990) 631.
8 Breslow, R. and Chung, S., Tetrahedron Lett., 30 (1989) 4353.
9 Breslow, R., Anslyn, E. and Huang, D.-L., Tetrahedron, 47 (1991) 2365.
10 Anslyn, E. and Breslow, R., J. Am. Chem. Soc., 111 (1989) 8931.
11 Weiner, W., Winkler, J., Zimmerman, S.C., Czarnik, A.W. and Breslow, R., J. Am. Chem. Soc., 107 (1985) 4093.
12 Breslow, R., Ciba Found. Symp., 158 (1991) 115.
13 Breslow, R., Pure Appl. Chem., 62 (1990) 1859.
14 D'Souza, V.T., Hanabusa, K., O'Leary, T., Gadwood, R.C. and Bender, M.L., Biochem. Biophys. Res. Commun., 129 (1985) 727.
15 Cucinotto, V., D'Allessandro, F., Impellizzeri, G., Pappalardo, G., Rizzarelli, E. and Vecchio, G., J. Chem. Soc., Chem. Commun., (1991) 293.
16 Menger, F.M. and Sherrod, M.J., J. Am. Chem. Soc., 110 (1988) 8606.
17 Cram, D.J. and Katz, H.E., J. Am. Chem. Soc., 105 (1983) 135.
18 Cram, D.J. and Lam, P.Y.-S., Tetrahedron, 42 (1986) 1607.
19 Cram, D.J., Lam, P.Y.-S. and Ho, S.P., J. Am. Chem. Soc., 108 (1986) 839.
20 Kellog, R.M., Kaptein, B. and Buter, J., Bull. Chem. Soc. Belg., 99 (1990) 703.
21 Tabushi, I., Kuroda, Y. and Mochizuchi, I., J. Am. Chem. Soc., 102 (1980) 1152.
22 Mallick, I.M., D'Souza, V.T., Yamaguchi, M., Lee, J., Chalabi, P., Gadwood, R.C. and Bender, M.L., J. Am. Chem. Soc., 106 (1984) 7252.
23 Gennari, C., Molinari, F., Piarulli, U. and Bartoletti, M., Tetrahedron, 46 (1990) 7289.
24 Gennari, C., Molinari, F. and Piarulli, U., Tetrahedron Lett., 31 (1990) 2929.
25 Mertes, M.P. and Mertes, K.M., Acc. Chem. Res., 23 (1990) 413.
26 Hahn, K.W., Klis, W.A. and Stewart, J.M., Science, 248 (1990) 1544.
27 Suh, J., Acc. Chem. Res., 25 (1992) 273.
28 Atassi, M.Z. and Manshouri, T., Proc. Natl. Acad. Sci. USA, 90 (1993) 8282.
29 Matthews, B.W., Craik, C.S. and Neurath, H., Proc. Natl. Acad. Sci. USA, 91 (1994) 4103.
30 Wells, J.A., Fairbrother, W.J., Otlewski, J. and Laskowski, J.M., Proc. Natl. Acad. Sci. USA, 91 (1994) 4110.
31 Corey, D.R. and Phillips, M.A., Proc. Natl. Acad. Sci. USA, 91 (1994) 4106.
32 Marrone, T.J. and McCammon, J.A., J. Am. Chem. Soc., 116 (1994) 6987.
33 Venanzi, C.A. and Bunce, J.D., Int. J. Quantum Chem., Quantum Biol. Symp., 12 (1986) 69.
34 Venanzi, C.A. and Bunce, J.D., Ann. New York Acad. Sci., 471 (1986) 318.
35 Venanzi, C.A. and Bunce, J.D., Enzyme, 36 (1986) 79.
36 Venanzi, C.A. and Namboodiri, K., Anal. Chim. Acta, 210 (1988) 151.
37 Venanzi, C.A., In Liebman, J.F. and Greenberg, A. (Eds.), Environmental Influences and Recognition in Enzyme Chemistry, Vol. 10, VCH, New York, NY, 1988, p. 251.
38 Venanzi, C.A., Canzius, P.M., Zhang, Z. and Bunce, J.D., J. Comput. Chem., 10 (1989) 1038.
39 Maye, P.V. and Venanzi, C.A., Struct. Chem., 1 (1990) 517.
40 Venanzi, C.A. and Maye, P.V., Struct. Chem., 2 (1991) 493.
41 Maye, P.V. and Venanzi, C.A., J. Comput. Chem., 12 (1991) 994.
42 Wertz, D.A., Shi, C.-X. and Venanzi, C.A., J. Comput. Chem., 13 (1992) 41.
43 Wallis, M., Howell, S.L. and Taylor, K.W., The Biochemistry of Polypeptide Hormones, Wiley, New York, NY, 1985.
44 Torda, A.E., Brunne, R.M., Huber, T., Kessler, H. and Van Gunsteren, W.F., J. Biomol. NMR, 3 (1993) 55.
45 Schwyzer, R., Ann. New York Acad. Sci., 297 (1977) 3.
46 Seelig, S., Sayers, G., Schwyzer, R. and Schiller, P., Febs Lett., 19 (1971) 232.
47 Fauchère, J.-L., Helv. Chim. Acta, 68 (1985) 770.
48 Fauchère, J.-L., Rossier, M., Capponi, A. and Vallotton, M.B., Febs Lett., 183 (1985) 283.
49 Fauchère, J.L. and Petermann, C., Helv. Chim. Acta, 61 (1978) 1186.
50 Bristow, A.F., Gleed, C., Fauchère, J.-L., Schwyzer, R. and Schulster, D., Biochem. J., 186 (1980) 599.
51 Patel, D.J., Macromolecules, 4 (1971) 251.
52 Toma, F., Fermandjian, S., Loew, M. and Kisfaludy, L., Biopolymers, 20 (1981) 901.
53 Schwyzer, R. and Kappeler, H., Helv. Chim. Acta, 44 (1961) 1991.
54 Kaptein, R., Boelens, R., Scheek, R.M. and Van Gunsteren, W.F., Biochemistry, 27 (1988) 5389.
55 Kaptein, R., Zuiderweg, E.R.P., Scheek, R.M., Boelens, R. and Van Gunsteren, W.F., J. Mol. Biol., 182 (1985) 179.
56 Zuiderweg, E.R.P., Scheek, R.M., Boelens, R., Van Gunsteren, W.F. and Kaptein, R., Biochemie, 67 (1985) 707.
57 De Vlieg, J., Boelens, R., Scheek, R.M., Kaptein, R. and Van Gunsteren, W.F., Isr. J. Chem., 27 (1986) 181.
58 De Vlieg, J., Scheek, R.M., Van Gunsteren, W.F., Berendsen,

H.J.C., Kaptein, R. and Thomason, J., Protein Struct. Funct. Genet., 3 (1988) 209.
59 Torda, A.E., Mabbutt, B.C., Van Gunsteren, W.F. and Norton, R.S., Febs Lett., 239 (1988) 266.
60 Kaluarachchi, K., Meadows, R.P. and Gorenstein, D.G., Biochemistry, 30 (1991) 8785.
61 Clore, G.M., Sukumaran, D.K., Nilges, M. and Gronenborn, A.M., Biochemistry, 26 (1987) 1732.
62 Chiche, L., Gaboriaud, C., Heitz, A., Mornon, J.-P., Castro, B. and Kollman, P.A., Protein Struct. Funct. Genet., 6 (1989) 405.
63 Lee, S.C., Russel, A.F. and Laidig, W.D., Int. J. Pept. Protein Res., 35 (1990) 367.
64 Baleja, J.D., Pon, R.T. and Sykes, B.D., Biochemistry, 29 (1990) 4828.
65 Schmidt, J.M., Ohlenschläger, O., Rüterjans, H., Grzonka, Z., Kojro, E., Pavo, I. and Fahrenholtz, F., Eur. J. Biochem., 201 (1991) 355.
66 Sanson, M.S.P., Son, H.S., Sankararamakrishnon, R., Kerr, I.D. and Breed, J., Biophys. J., 65 (1995) 1295.
67 Kessler, H., Bats, J.W., Griesinger, C., Koll, S., Will, M. and Wagner, K., J. Am. Chem. Soc., 110 (1991) 1033.
68 Lautz, J., Kessler, H., Kaptein, R. and Van Gunsteren, W.F., J. Comput.-Aided Mol. Design, 1 (1987) 219.
69 Lautz, J., Kessler, H., Boelens, R., Kaptein, R. and Van Gunsteren, W.F., Int. J. Pept. Protein Res., 30 (1987) 404.
70 Pepermans, H., Tourwé, D., Van Binst, G., Boelens, R., Scheek, R., Van Gunsteren, W.F. and Kaptein, R., Biopolymers, 27 (1988) 323.
71 Fesik, S.W., Bolis, G., Sham, H.L. and Olejniczak, E.T., Biochemistry, 26 (1987) 1851.
72 Fry, D.C., Madison, V.S., Greeley, D.N., Felix, A.M., Heimer, E.P., Frohman, L., Campbell, R.M., Mowles, T.F., Toome, V. and Wegrzynski, B.B., Biopolymers, 32 (1992) 649.
73 Saulitis, J., Mierke, D.F., Byk, G., Gilon, C. and Kessler, H., J. Am. Chem. Soc., 114 (1992) 4818.
74 Mierke, D.F., Pattaroni, C., Delaet, N., Toy, A., Goodman, M., Tancredi, T., Motta, A., Temussi, P.A., Moroder, L., Bovermann, G. and Wünsch, E., Int. J. Pept. Protein Res., 36 (1990) 418.
75 Jayaraman, G., Bhaskaran, R., Kumar, T.K.S., Yu, H.-M., Chen, S.-T. and Yu, C., Int. J. Pept. Protein Res., 46 (1995) 88.
76 Ma, S., McGregor, M.J., Cohen, F.E. and Pallai, P.V., Biopolymers, 34 (1994) 987.
77 Beusen, D.D., Zabrocki, J., Slomczynska, U., Head, R.D., Kao, J.L.-F. and Marshall, G.R., Biopolymers, 36 (1995) 181.
78 Van Gunsteren, W.F. and Berendsen, H.J.C., available from Biomos B.V., Groningen, The Netherlands.
79 Torda, A.E., Scheek, R.M. and Van Gunsteren, W.F., Chem. Phys. Lett., 157 (1989) 289.
80 Torda, A.E., Scheek, R.M. and Van Gunsteren, W.F., J. Mol. Biol., 214 (1990) 223.
81 Scheek, R.M., Torda, A.E., Kemmink, J. and Van Gunsteren, W.F., In Hoch, J.C., Poulson, F.M. and Redfield, C. (Eds.) Computational Aspects of the Study of Biological Macromolecules by Nuclear Magnetic Resonance, Plenum, New York, NY, 1991, p. 209.
82 Nanzer, A.P., Poulsen, F.M., Van Gunsteren, W.F. and Torda, A.E., Biochemistry, 33 (1994) 14503.
83 Kessler, H., Matter, H., Gemmecker, G., Kling, A. and Kottenhahn, M., J. Am. Chem. Soc., 113 (1991) 7550.
84 Kessler, H., Matter, H., Gemmecker, G., Kottenhahn, M. and Bats, J.W., J. Am. Chem. Soc., 114 (1992) 4805.
85 Mierke, D.F., Huber, T. and Kessler, H., J. Comput.-Aided Mol. Design, 8 (1994) 29.
86 Brunne, R.M. and Liebfritz, D., Int. J. Pept. Protein Res., 40 (1992) 401.
87 Barany, G. and Merrifield, R.B., In Gross, E. and Meienhofer, J. (Eds.), The Peptides, Analysis, Synthesis, Biology, Vol. 2, Academic Press, London, U.K., 1979, p. 1.
88 Fields, G.B. and Noble, R.L., Int. J. Pept. Protein Res., 35 (1990) 161.
89 Mergler, M., Tanner, R., Gosteli, J. and Grogg, P., Tetrahedron Lett., 29 (1988) 4005.
90 Castro, B., Dormoy, J.R., Evin, G. and Selve, C., Tetrahedron Lett., 14 (1975) 1219.
91 Macura, S. and Ernst, R.R., Mol. Phys., 41 (1980) 95.
92 Bax, A. and Davis, D.G., J. Magn. Reson., 65 (1985) 355.
93 Bax, A. and Davis, D.G., J. Magn. Reson., 63 (1985) 207.
94 Wüthrich, K., NMR of Proteins and Nucleic Acids, Wiley, New York, NY, 1986.
95 Van Nuland, N.A.J., Groetzinger, J., Dijkstra, K., Scheek, R.M. and Robillard, G.T., Eur. J. Biochem., 210 (1992) 881.
96 Crippen, G.M. and Havel, T.F., Acta Crystallogr., A34 (1978) 282.
97 Scheek, R.M., Van Gunsteren, W.F. and Kaptein, R., Methods Enzymol., 177 (1989) 204.
98 Available from Molecular Simulations, Boston, MA.
99 Van Gunsteren, W.F. and Berendsen, H.J.C., Mol. Phys., 34 (1977) 1311.
100 Berendsen, H.J.C., Postma, J.P.M., Van Gunsteren, W.F., DiNola, A. and Haak, J.R., J. Chem. Phys., 81 (1984) 3684.
101 Berendsen, H.J.C., Van Gunsteren, W.F., Zwinderman, H.R. and Geurtsen, R.G., Ann. New York Acad. Sci., 482 (1986) 269.
102 Kern, P., Brunne, R.M. and Folkers, G., J. Comput.-Aided Mol. Design, 8 (1994) 367.
103 Van Gunsteren, W.F., Boelens, R., Kaptein, R., Scheek, R.M. and Zuiderweg, E.R.P., In Hermans, J. (Ed.), Molecular Dynamics and Protein Structure, Polycrystal Book Service, Western Springs, IL, 1985, p. 92.
104 Developed and distributed by Chemical Design, Ltd., Oxford, U.K.
105 Beveridge, D.L., McConnell, K.J., Nirmala, R., Young, M.A., Vijayakumar, S. and Ravishanker, G., In Cramer, C.J. and Truhlar, D.G. (Eds.) Structure and Reactivity in Aqueous Solution, ACS Symposium Series Vol. 568, American Chemical Society, Washington, DC, 1995, p. 381.
106 Pearlman, D.A., J. Biomol. NMR, 4 (1994) 279.
107 Tsukada, H. and Blow, D.M., J. Mol. Biol., 184 (1985) 703.
108 Blevins, R.A. and Tulinsky, A., J. Biol. Chem., 260 (1985) 4264.
109 Pearlman, D.A. and Kollman, P.A., J. Mol. Biol., 220 (1991) 457.
110 Pearlman, D.A., J. Biomol. NMR, 4 (1994) 1.
111 Schmitz, U., Kumar, A. and James, T.L., J. Am. Chem. Soc., 114 (1992) 10654.
112 Gandour, R.D., Bioorg. Chem., 10 (1981) 169.
113 Rebek, J.J., In Liebman, J.F. and Greenberg, A. (Eds.), Environmental Influences and Recognition in Enzyme Chemistry, Vol. 10, VCH, New York, NY, 1988, p. 219.
114 Li, Y. and Houk, K.N., J. Am. Chem. Soc., 111 (1989) 4505.
115 Rebek, J., Struct. Chem., 1 (1990) 129.
116 Corey, D.R., McGrath, M.E., Vasquez, J.R., Fletterick, R.J. and Craik, C.S., J. Am. Chem. Soc., 114 (1992) 4905.
117 Corey, D.R. and Craik, C.S., J. Am. Chem. Soc., 114 (1992) 1784.
118 D'Souza, V.T. and Bender, M.L., Acc. Chem. Res., 20 (1987) 146.